

## On the Influence of Random Wind Stress Errors on the Four-Dimensional, Midlatitude Ocean Inverse Problem

TSUYOSHI WAKAMATSU,\* MICHAEL G. G. FOREMAN,\* PATRICK F. CUMMINS, AND JOSEF Y. CHERNIAWSKY

*Fisheries and Oceans Canada, Institute of Ocean Sciences, Sidney, British Columbia, Canada*

(Manuscript received 11 April 2008, in final form 28 November 2008)

### ABSTRACT

The effects of the parameterized wind stress error covariance function on the a priori error covariance of an ocean general circulation model (OGCM) are examined. These effects are diagnosed by computing the projection of the a priori model state error covariance matrix to sea surface height (SSH). The sensitivities of the a priori error covariance to the wind stress curl error are inferred from the a priori SSH error covariance and are shown to differ between the subpolar and subtropical gyres because of different contributions from barotropic and baroclinic ocean dynamics. The spatial structure of the SSH error covariance due to the wind stress error indicates that the a priori model state error is determined indirectly by the wind stress curl error. The impact of this sensitivity on the solution of a four-dimensional inverse problem is inferred.

### 1. Introduction

An advanced data assimilation technique for four-dimensional (4D) ocean data assimilation studies seeks an optimal trajectory of a model state vector by estimating errors in the model equations, initial values, boundary values, and constants in the subgrid-scale parameterization schemes. The four-dimensional variational data assimilation (4DVAR) techniques with strong/weak constraints are the most common techniques to solve this type of inverse problem. In these techniques, the optimal sizes of errors are sought by minimizing a cost function that requires knowledge of the statistical properties of those errors. Generally, estimating an adequate structure for the statistical properties is not a trivial task and we need to model them with certain assumptions. In this study, we investigate the impact of the assumptions we make for the wind stress error covariance function in estimating wind-driven basin-scale ocean circulation.

The statistical properties of the wind stress error are introduced into 4DVAR and Kalman filter/smoothing data assimilation systems as a model error covariance matrix. The simplest formulation is based on the assumptions that the zonal and meridional wind stress errors are independent stochastic processes and that their autocovariance functions can be modeled as a diagonal matrix (e.g., Stammer et al. 2002, 2003; Masuda et al. 2003; Köhl et al. 2007). When we interpret the error covariance matrix in terms of its power spectrum distribution (e.g., Priestley 1981), the diagonal covariance assumption indicates that the error signal is a white noise process. Although there is no direct evidence indicating that the wind stress error can be modeled by a white noise process, nondiagonal forms of the wind stress error covariance matrix are seldom used in 4D ocean data assimilation. Vossepoel et al. (2004) implemented a nondiagonal wind stress error covariance matrix in the 4DVAR system in their twin experiments. In the Kalman filter technique, Miller and Cane (1989) assumed a Gaussian function to design the wind stress error covariance while Fukumori et al. (1999) used a nondiagonal wind stress error covariance model based on sample covariance calculated from reanalysis wind stress data.

Since the wind stress error is a stochastic variable, its impact on the analysis of 4D data assimilation may be understood by looking at the response of the wind-driven ocean circulation to a stochastic wind stress

---

\* Additional affiliation: School of Earth and Ocean Sciences, University of Victoria, Victoria, British Columbia, Canada.

---

Corresponding author address: Tsuyoshi Wakamatsu, Fisheries and Oceans Canada, Institute of Ocean Sciences, 9860 West Saanich Rd., P.O. Box 6000, Sidney BC V8L 4B2, Canada.  
E-mail: tsuyoshi.wakamatsu@dfo-mpo.gc.ca

forcing. The statistical properties of the ocean state vector in relation to the stochastic wind stress have been studied extensively since the pioneering works of Veronis and Stommel (1956) and Veronis (1970). Frankignoul et al. (1997), Willebrand et al. (1980), and Müller and Frankignoul (1981) examined the linear quasigeostrophic response of the midlatitude ocean to a stochastic wind stress and suggested that the synoptic to basin-scale ocean response is largely controlled by the wind stress curl. However, in modern data assimilation systems based on primitive equations, error statistics of the wind stress curl error are not explicitly mentioned and their impact on the inverse solution is not well understood.

In this study, we investigate the role of the wind stress error term in shaping the optimal solution of a 4DVAR data assimilation system applied to midlatitude, basin-scale ocean circulation. Specifically, we investigate the impact of wind stress curl error statistics, which are implicitly determined by the wind stress error statistics, on the 4DVAR analysis. This paper is organized as follows. In section 2, the role of the model error in a variational data assimilation system is explored, while section 3 describes a wind stress curl and divergence error that are implicitly specified by a given wind stress error covariance. The experimental design to examine the sensitivity of the a priori model state error covariance matrix to the correlation structure of a wind stress error is described in section 4. The results obtained from the numerical experiments are discussed in section 5 and concluding remarks are given in section 6.

## 2. Review of a 4DVAR system

Various types of 4DVAR techniques, such as strong or weakly constrained 4DVAR and the representer method are all based on the maximum a posteriori probability (MAP) estimation (e.g., Todling 2000). Let a vector  $\mathbf{x}$  denote the 4D model state vector to be estimated in the data assimilation system. Given a data vector  $\mathbf{y}$  as a linear transformation of  $\mathbf{x}$ , the MAP estimation of  $\mathbf{x}$  is obtained by minimizing the cost function defined as

$$J[\mathbf{x}] = \frac{1}{2}(\mathbf{x} - \mathbf{x}^b)^T \mathbf{P}^{-1}(\mathbf{x} - \mathbf{x}^b) + \frac{1}{2}(\mathbf{y} - \mathbf{H}\mathbf{x})^T \mathbf{R}^{-1}(\mathbf{y} - \mathbf{H}\mathbf{x}), \tag{1}$$

where  $\mathbf{x}^b$  is the background or the first-guess estimation of  $\mathbf{x}$ ,  $\mathbf{H}$  is the observation matrix,  $\mathbf{R}$  is the observation error covariance matrix, and the superscript T indicates transpose.

The a priori model state error covariance matrix  $\mathbf{P}$  is defined as

$$\mathbf{P} = \langle (\mathbf{x}^t - \mathbf{x}^b)(\mathbf{x}^t - \mathbf{x}^b)^T \rangle, \tag{2}$$

where  $\langle \rangle$  is the statistical mean operator,  $\mathbf{x}^t$  denotes true model state, and  $\mathbf{x}^b$  is assumed to be unbiased ( $\langle \mathbf{x}^t - \mathbf{x}^b \rangle = 0$ ). The MAP estimate of  $\mathbf{x}$  is readily derived from (1) in the same manner as the optimal interpolation (OI) system (e.g., Courtier 1997); namely,

$$\mathbf{x}^a = \mathbf{x}^b + \mathbf{P}\mathbf{H}^T(\mathbf{S} + \mathbf{R})^{-1} \mathbf{d}, \tag{3}$$

where  $\mathbf{S} = \mathbf{H}\mathbf{P}\mathbf{H}^T$  is the representer matrix and  $\mathbf{d} = \mathbf{y} - \mathbf{H}\mathbf{x}^b$  is the innovation vector. The role of  $\mathbf{P}$  in finding the optimal estimation  $\mathbf{x}^a$  is to determine the shape of the interpolation kernels that redistribute the model–data misfits in  $\mathbf{d}$  to their surrounding four-dimensional space (Bennett 1992, 2002).

The formulation of the 4DVAR algorithm starts by defining a cost function of the form

$$J[\mathbf{x}] = \frac{1}{2} \mathbf{u}^T \mathbf{Q}^{-1} \mathbf{u} + \frac{1}{2} (\mathbf{y} - \mathbf{H}\mathbf{x})^T \mathbf{R}^{-1} (\mathbf{y} - \mathbf{H}\mathbf{x}) \tag{4}$$

with dynamical constraints

$$G[\mathbf{x}] - \mathbf{f} = \mathbf{u}, \tag{5}$$

where  $G$  is the (non)linear model operator;  $\mathbf{f}$  is the background estimation of forcing, which may include external forcing, internal sources, and boundary and initial values; and  $\mathbf{u}$  is the error in the model equations with a covariance matrix  $\langle \mathbf{u}\mathbf{u}^T \rangle = \mathbf{Q}$  and a mean  $\langle \mathbf{u} \rangle = 0$ . The tangent linear approximation of (5) is

$$\mathbf{G}\mathbf{x} - \tilde{\mathbf{f}} = \mathbf{u}, \tag{6}$$

where  $\mathbf{G}$  is the tangent linear approximation of  $G$  linearized around the previous estimation of  $\mathbf{x}$  and  $\tilde{\mathbf{f}}$  is the extended forcing that includes  $\mathbf{f}$  and the pseudoforcing arising from the linearization of  $G$  (Ngodock et al. 2000).

Defining the background estimation  $\mathbf{x}^b$  as the solution of (6) when  $\mathbf{u} = 0$ , the incremental form of the tangent linear equation is written as

$$\mathbf{G}\delta\mathbf{x} = \mathbf{u}, \tag{7}$$

where  $\delta\mathbf{x} = \mathbf{x} - \mathbf{x}^b$ . Since the matrix  $\mathbf{G}$  is always invertible, we also have an alternative form of the tangent linear equation

$$\delta\mathbf{x} = \mathbf{M}\mathbf{u}, \tag{8}$$

where  $\mathbf{M} = \mathbf{G}^{-1}$  (see appendix A). From the expression in (8), it can be shown that the increment  $\delta\mathbf{x}$  has zero mean and its covariance is given by

$$\tilde{\mathbf{P}} \equiv \langle \delta\mathbf{x}\delta\mathbf{x}^T \rangle = \mathbf{M}\mathbf{Q}\mathbf{M}^T. \tag{9}$$

Inserting the left-hand side of (7) into  $\mathbf{u}$  on the right-hand side of (4), we obtain a cost function of the following form (see appendix A):

$$J[\delta\mathbf{x}] = \frac{1}{2}\delta\mathbf{x}^T\tilde{\mathbf{P}}^{-1}\delta\mathbf{x} + \frac{1}{2}(\mathbf{d} - \mathbf{H}\delta\mathbf{x})^T\mathbf{R}^{-1}(\mathbf{d} - \mathbf{H}\delta\mathbf{x}). \quad (10)$$

The minimum point of the cost function (10) is given by

$$\delta\mathbf{x}^a = \tilde{\mathbf{P}}\mathbf{H}^T(\tilde{\mathbf{S}} + \mathbf{R})^{-1}\mathbf{d}, \quad (11)$$

where  $\tilde{\mathbf{S}} \equiv \mathbf{H}\tilde{\mathbf{P}}\mathbf{H}^T$ . Equations (10) and (11) are the approximations of (1) and (3), respectively, in the outer loop of the 4DVAR algorithm. We expect that the covariance matrix  $\tilde{\mathbf{P}}$  in (10) converges to the a priori error covariance matrix  $\mathbf{P}$  in (1) at the end of the outer loop iterations. Thus, (9) and (10) indicate that the a priori error covariance matrix of 4DVAR is modeled by  $\mathbf{Q}$  and  $\mathbf{M}$  (Lorenz 2003). Assuming that  $\tilde{\mathbf{P}}$  at the first iteration is a good approximation of  $\mathbf{P}$ , we use the relation (9) as a tool to examine dependencies of a shape of  $\mathbf{P}$  on  $\mathbf{Q}$  in this study.

In 4DVAR ocean data assimilation, the first term of the cost function (4) typically has the following form (e.g., Stammer et al. 2002):

$$\mathbf{u}^T\mathbf{Q}^{-1}\mathbf{u} = \Delta\boldsymbol{\tau}^T\mathbf{Q}_{\Delta\tau}^{-1}\Delta\boldsymbol{\tau} + \Delta\mathbf{q}^T\mathbf{Q}_{\Delta q}^{-1}\Delta\mathbf{q} + \Delta\mathbf{x}_0^T\mathbf{B}^{-1}\Delta\mathbf{x}_0 + \Delta\mathbf{x}_B^T\mathbf{D}^{-1}\Delta\mathbf{x}_B + \Delta\mathbf{e}^T\mathbf{Q}_{\Delta e}^{-1}\Delta\mathbf{e}, \quad (12)$$

where  $\mathbf{u}^T = [\Delta\boldsymbol{\tau}^T, \Delta\mathbf{q}^T, \Delta\mathbf{x}_0^T, \Delta\mathbf{x}_B^T, \Delta\mathbf{e}^T]$  contains the errors in wind stress  $\Delta\boldsymbol{\tau}$ , the surface buoyancy flux  $\Delta\mathbf{q}$ , the initial values  $\Delta\mathbf{x}_0$ , the boundary values  $\Delta\mathbf{x}_B$ , and the internal model dynamics  $\Delta\mathbf{e}$ . Each of these error components is assumed to be an independent stochastic variable. Thus, the model error covariance matrix  $\mathbf{Q}$  on the left-hand side of (12) is a block diagonal matrix with submatrices  $\mathbf{Q}_{\Delta\tau}$ ,  $\mathbf{Q}_{\Delta q}$ ,  $\mathbf{B}$ ,  $\mathbf{D}$ , and  $\mathbf{Q}_{\Delta e}$  on the right-hand side. To focus on the role of the wind stress error constraint [the first term on the right-hand side of (12)] in the 4DVAR analysis, we will ignore all other errors in this study.

The impact of  $\mathbf{Q}$  on the shape of optimal estimation  $\mathbf{x}^a$  can be investigated by examining the dependency of  $\tilde{\mathbf{P}}$  on  $\mathbf{Q}$  in (9). Since the full matrix  $\tilde{\mathbf{P}}$  is too large to be evaluated directly, we use subspaces of  $\tilde{\mathbf{P}}$ . In particular, we use the column vector of  $\tilde{\mathbf{P}}$  that contains the cross

covariance between the sea surface height (SSH) error at a particular sample point and other model state errors. Since the SSH has strong sensitivity to stochastic wind stress (e.g., Willebrand et al. 1980), this column vector is expected to provide a good representation of  $\tilde{\mathbf{P}}$ . From (9), the column vector of  $\tilde{\mathbf{P}}$  that contains the cross covariance between the SSH error at the  $m$ th sample point ( $\mathbf{r}_m, t_m$ ), and the model state error is given by

$$\mathbf{p}_m^\eta = \langle (\mathbf{x} - \mathbf{x}^b)(\eta_m - \eta_m^b) \rangle, \quad (13)$$

where  $\eta_m \equiv \eta(\mathbf{r}_m, t_m)$  is the model SSH at a sample location  $\mathbf{r}_m$  over the sea surface and at a sample time  $t_m$ . The actual calculation of  $\mathbf{p}_m^\eta$  is conducted by replacing the statistical mean operator  $\langle \rangle$  by an ensemble mean operator  $\langle \rangle_N$  based on  $N$  realizations of  $\mathbf{x}$  calculated from (6).

An alternative method to calculate  $\mathbf{p}_m^\eta$  is to use the direct representer method (Bennett 1992). Using the alternative form of  $\tilde{\mathbf{P}}$  in (9), it can be shown that  $\mathbf{p}_m^\eta$  is evaluated by

$$\mathbf{p}_m^\eta = \mathbf{M}\mathbf{Q}\mathbf{M}^T\mathbf{h}_m^\eta, \quad (14)$$

where, the column vector  $\mathbf{h}_m^\eta$  is defined such that  $\eta_m$  is extracted from  $\mathbf{x}$  by  $\eta_m = (\mathbf{h}_m^\eta)^T\mathbf{x}$ . Equation (14) can be evaluated in the following two steps:

$$\boldsymbol{\lambda} = \mathbf{M}^T\mathbf{h}_m^\eta \quad \text{and} \quad (15)$$

$$\mathbf{p}_m^\eta = \mathbf{M}\mathbf{Q}\boldsymbol{\lambda}, \quad (16)$$

where  $\boldsymbol{\lambda}$  is the adjoint variable vector. Equation (15) is the adjoint backward equation and (16) is the tangent linear forward equation (Bennett 2002, p. 19). We refer to  $\mathbf{p}_m^\eta$  as a representer vector hereafter in this study. If we use an infinite number of realizations to compute (13), the two methods in (13) and (14) lead to the same solution. For cross-validation purposes, we use both methods to compute  $\mathbf{p}_m^\eta$ .

### 3. Wind stress error covariance function

The covariance of the wind stress error vector,  $\Delta\boldsymbol{\tau} = [\Delta\tau_x, \Delta\tau_y]^T$ , can be expressed by the bivariate covariance matrix:

$$\mathbf{Q}_{\Delta\tau}(\mathbf{r}_1, t_1; \mathbf{r}_2, t_2) \equiv \langle \Delta\boldsymbol{\tau}(\mathbf{r}_1, t_1)\Delta\boldsymbol{\tau}(\mathbf{r}_2, t_2)^T \rangle = \begin{bmatrix} Q_{\Delta\tau}^{xx}(\mathbf{r}_1, t_1; \mathbf{r}_2, t_2) & Q_{\Delta\tau}^{xy}(\mathbf{r}_1, t_1; \mathbf{r}_2, t_2) \\ Q_{\Delta\tau}^{yx}(\mathbf{r}_1, t_1; \mathbf{r}_2, t_2) & Q_{\Delta\tau}^{yy}(\mathbf{r}_1, t_1; \mathbf{r}_2, t_2) \end{bmatrix}, \quad (17)$$

where  $\mathbf{r} = (x, y)$  is a location over the sea surface, and  $t$  is a time coordinate. Auto- and cross-covariance functions on the right-hand side of (17) are defined by

$$Q_{\Delta\tau}^{ab}(\mathbf{r}_1, t_1; \mathbf{r}_2, t_2) \equiv \langle \Delta\tau_a(\mathbf{r}_1, t_1) \Delta\tau_b(\mathbf{r}_2, t_2) \rangle. \quad (18)$$

For simplification, we have also assumed that  $\langle \Delta\tau \rangle = 0$ . The covariance matrix  $\mathbf{Q}_{\Delta\tau}$  is normally simplified in 4DVAR ocean data assimilation studies. In the following, we will review typical simplifications and discuss their consequences from a dynamical point of view.

In subsequent discussions, we assume that the cross-covariance components,  $Q_{\Delta\tau}^{xy}$  and  $Q_{\Delta\tau}^{yx}$ , in (17) are zero, meaning that the zonal and meridional wind stress errors are independent, stochastic variables. The general case with nonzero cross-covariance functions is discussed in appendix B. Under this assumption, the cost function that measures a size of the wind stress error is written in the following form:

$$J_{\Delta\tau}[\Delta\tau_x, \Delta\tau_y] = \frac{1}{2} \Delta\tau_x \bullet W_{\Delta\tau}^x \bullet \Delta\tau_x + \frac{1}{2} \Delta\tau_y \bullet W_{\Delta\tau}^y \bullet \Delta\tau_y, \quad (19)$$

where  $\bullet$  is the inner product defined as

$$\alpha \bullet \beta = \iiint \alpha(\mathbf{r}, t) \beta(\mathbf{r}, t) \, d\mathbf{r} \, dt, \quad (20)$$

and  $W_{\Delta\tau}^{x(y)}$  is the weight function that satisfies

$$Q_{\Delta\tau}^{xx(yy)}(\mathbf{r}_1, t_1; \mathbf{r}_2, t_2) \bullet W_{\Delta\tau}^{x(y)}(\mathbf{r}_1, t_1; \mathbf{r}_2, t_2) = \delta(\mathbf{r}_1 - \mathbf{r}_2, t_1 - t_2). \quad (21)$$

The right-hand side of (21) is the Dirac delta function.

We also assume that  $\Delta\tau$  is a stationary stochastic process, which can be expressed by the following form:

$$\begin{aligned} \Delta\tau &= [\Delta\tau_x(\mathbf{r}, t), \Delta\tau_y(\mathbf{r}, t)] \\ &= [\sigma_{\Delta\tau}^x(\mathbf{r}) \Delta\hat{\tau}_x(\mathbf{r}, t), \sigma_{\Delta\tau}^y(\mathbf{r}) \Delta\hat{\tau}_y(\mathbf{r}, t)], \end{aligned} \quad (22)$$

where  $\sigma_{\Delta\tau}^{x(y)}$  is the standard deviation and  $\Delta\hat{\tau}_{x(y)}$  is the normalized wind stress error of the zonal (meridional) component with unit variance. We further assume that the stochastic process of  $\Delta\hat{\tau}_{x(y)}$  is uniform and its correlation function is separable in spatial and temporal coordinates. Then the autocovariance functions on the right-hand side of (17) can be written as

$$\begin{aligned} Q_{\Delta\tau}^{xx}(\mathbf{r}_1, t_1; \mathbf{r}_2, t_2) &= \sigma_{\Delta\tau}^x(\mathbf{r}_1) \rho_{\Delta\tau}^x(\tilde{\mathbf{r}}) \rho_{\Delta\tau}^x(\tilde{t}) \sigma_{\Delta\tau}^x(\mathbf{r}_2) \quad \text{and} \\ Q_{\Delta\tau}^{yy}(\mathbf{r}_1, t_1; \mathbf{r}_2, t_2) &= \sigma_{\Delta\tau}^y(\mathbf{r}_1) \rho_{\Delta\tau}^y(\tilde{\mathbf{r}}) \rho_{\Delta\tau}^y(\tilde{t}) \sigma_{\Delta\tau}^y(\mathbf{r}_2), \end{aligned} \quad (23)$$

where

$$\begin{aligned} \rho_{\Delta\tau}^{x(y)}(\tilde{\mathbf{r}}) \rho_{\Delta\tau}^t(\tilde{t}) &\equiv \langle \Delta\hat{\tau}_{x(y)}(\mathbf{r}_1, t_1) \Delta\hat{\tau}_{x(y)}(\mathbf{r}_2, t_2) \rangle, \quad \tilde{\mathbf{r}} \equiv \mathbf{r}_2 - \mathbf{r}_1, \\ \tilde{t} &\equiv t_2 - t_1. \end{aligned}$$

In (23) we have also assumed that the zonal and meridional wind stress errors have the same temporal correlation function  $\rho_{\Delta\tau}^t(\tilde{t})$ .

Wind-driven ocean circulation is controlled by the rotational (curl) and irrotational (divergence) components in the wind stress field. The dynamical impact of the wind stress error structure on 4DVAR analysis can be better understood by examining the error structure of these effective forcing terms (i.e., wind stress curl and divergence errors) rather than wind stress error. The wind stress curl error,  $\Delta\mathbf{s}$ , and divergence error,  $\Delta\mu$ , are calculated from the given wind stress error as

$$\Delta\mathbf{s} \equiv \frac{\partial \Delta\tau_y}{\partial x} - \frac{\partial \Delta\tau_x}{\partial y} \quad \text{and} \quad (24)$$

$$\Delta\mu \equiv \frac{\partial \Delta\tau_x}{\partial x} + \frac{\partial \Delta\tau_y}{\partial y}. \quad (25)$$

From (24) and (25), the covariance functions of  $\Delta\mathbf{s}$  and  $\Delta\mu$  can be expressed by the covariance functions of original wind stress errors as

$$\mathbf{Q}_{\text{eff}} = \begin{bmatrix} Q_{\Delta\mathbf{s}\Delta\mathbf{s}} & Q_{\Delta\mathbf{s}\Delta\mu} \\ Q_{\Delta\mu\Delta\mathbf{s}} & Q_{\Delta\mu\Delta\mu} \end{bmatrix} = F[\mathbf{Q}_{\Delta\tau}]. \quad (26)$$

Inversely, we also have

$$\mathbf{Q}_{\Delta\tau} = F^{-1}[\mathbf{Q}_{\text{eff}}]. \quad (27)$$

The explicit forms of the functionals  $F$  in Eq. (26) and  $F^{-1}$  in Eq. (27) are discussed in appendix B. Since  $\tilde{\mathbf{P}}$  is a function of  $\mathbf{Q}_{\Delta\tau}$  as indicated by (9),  $\tilde{\mathbf{P}}$  can also be parameterized as a function of the effective forcing error covariance  $\mathbf{Q}_{\text{eff}}$ .

In the following discussion, we will focus on the structure of the wind stress curl error covariance function,  $Q_{\Delta\mathbf{s}\Delta\mathbf{s}}$ . From (22) and (24), we obtain

$$\Delta\mathbf{s} = \Delta\mathbf{s}_{\partial\sigma} + \Delta\mathbf{s}_{\partial\tau}, \quad (28)$$

where

$$\begin{aligned} \Delta\mathbf{s}_{\partial\sigma} &\equiv \frac{\partial \sigma_{\Delta\tau}^y}{\partial x} \Delta\hat{\tau}_y - \frac{\partial \sigma_{\Delta\tau}^x}{\partial y} \Delta\hat{\tau}_x \quad \text{and} \\ \Delta\mathbf{s}_{\partial\tau} &\equiv \sigma_{\Delta\tau}^y \frac{\partial \Delta\hat{\tau}_y}{\partial x} - \sigma_{\Delta\tau}^x \frac{\partial \Delta\hat{\tau}_x}{\partial y}. \end{aligned} \quad (29)$$

We have assumed that  $\sigma_{\Delta\tau}^{x(y)}$  and  $\Delta\hat{\tau}_{x(y)}$  are differentiable at least to the first order. The wind stress curl error  $\Delta\mathbf{s}$  consists of two terms. The first term originates from the

shear of the wind stress error standard deviations, while the second term originates from the shear of the normalized wind stress error field.

From (28), the autocovariance function  $Q_{\Delta s \Delta s}$  has another representation as

$$Q_{\Delta s \Delta s} = Q_{\Delta s \Delta s}^{\partial \sigma \partial \sigma} + Q_{\Delta s \Delta s}^{\partial \tau \partial \tau} + Q_{\Delta s \Delta s}^{\partial \sigma \partial \tau} + Q_{\Delta s \Delta s}^{\partial \tau \partial \sigma}, \quad (30)$$

where

$$\begin{aligned} Q_{\Delta s \Delta s}^{\partial \sigma \partial \sigma} &\equiv \langle \Delta \mathbf{s}_{\partial \sigma}(\mathbf{r}_1, t_1) \Delta \mathbf{s}_{\partial \sigma}(\mathbf{r}_2, t_2) \rangle, \\ Q_{\Delta s \Delta s}^{\partial \tau \partial \tau} &\equiv \langle \Delta \mathbf{s}_{\partial \tau}(\mathbf{r}_1, t_1) \Delta \mathbf{s}_{\partial \tau}(\mathbf{r}_2, t_2) \rangle, \\ Q_{\Delta s \Delta s}^{\partial \sigma \partial \tau} &\equiv \langle \Delta \mathbf{s}_{\partial \sigma}(\mathbf{r}_1, t_1) \Delta \mathbf{s}_{\partial \tau}(\mathbf{r}_2, t_2) \rangle, \quad \text{and} \\ Q_{\Delta s \Delta s}^{\partial \tau \partial \sigma} &\equiv \langle \Delta \mathbf{s}_{\partial \tau}(\mathbf{r}_1, t_1) \Delta \mathbf{s}_{\partial \sigma}(\mathbf{r}_2, t_2) \rangle. \end{aligned} \quad (31)$$

From (29) and (31),  $Q_{\Delta s \Delta s}^{\partial \sigma \partial \sigma}$  is written as

$$\begin{aligned} Q_{\Delta s \Delta s}^{\partial \sigma \partial \sigma}(\mathbf{r}_1, t_1; \mathbf{r}_2, t_2) &= \left[ \frac{\partial \sigma_{\Delta \tau}^x(\mathbf{r}_1)}{\partial y} \rho_{\Delta \tau}^x(\tilde{\mathbf{r}}) \frac{\partial \sigma_{\Delta \tau}^x(\mathbf{r}_2)}{\partial y} \right. \\ &\quad \left. + \frac{\partial \sigma_{\Delta \tau}^y(\mathbf{r}_1)}{\partial x} \rho_{\Delta \tau}^y(\tilde{\mathbf{r}}) \frac{\partial \sigma_{\Delta \tau}^y(\mathbf{r}_2)}{\partial x} \right] \rho_{\Delta \tau}^t(\tilde{t}), \end{aligned} \quad (32)$$

where  $\rho_{\Delta \tau}^{x(y)}$  is the correlation function of  $\Delta \tau_{x(y)}$  and we used the assumption that  $\Delta \tau_x$  and  $\Delta \tau_y$  are independent stochastic variables. Assuming that the correlation functions  $\rho_{\Delta \tau}^x$  and  $\rho_{\Delta \tau}^y$  are twice differentiable,  $Q_{\Delta s \Delta s}^{\partial \tau \partial \tau}$  is written as

$$\begin{aligned} Q_{\Delta s \Delta s}^{\partial \tau \partial \tau}(\mathbf{r}_1, t_1; \mathbf{r}_2, t_2) &= \left\{ \sigma_{\Delta \tau}^x(\mathbf{r}_1) \left[ -\frac{\partial^2 \rho_{\Delta \tau}^x(\tilde{\mathbf{r}})}{\partial \tilde{y}^2} \right] \sigma_{\Delta \tau}^x(\mathbf{r}_2) \right. \\ &\quad \left. + \sigma_{\Delta \tau}^y(\mathbf{r}_1) \left[ -\frac{\partial^2 \rho_{\Delta \tau}^y(\tilde{\mathbf{r}})}{\partial \tilde{x}^2} \right] \sigma_{\Delta \tau}^y(\mathbf{r}_2) \right\} \rho_{\Delta \tau}^t(\tilde{t}). \end{aligned} \quad (33)$$

We consider the case when the first derivatives of the autocorrelation functions  $\rho_{\Delta \tau}^x$  and  $\rho_{\Delta \tau}^y$  vanish at  $\tilde{\mathbf{r}} = 0$ , which is true for the Gaussian function used in this study. In this case, the cross-covariance functions,  $Q_{\Delta s \Delta s}^{\partial \sigma \partial \tau}$  and  $Q_{\Delta s \Delta s}^{\partial \tau \partial \sigma}$ , on the right-hand side of (30) do not contribute to the variance distributions of  $\Delta \mathbf{s}$ . Then the variance of the wind stress curl error is deduced from (30), (32), and (33) as

$$\begin{aligned} \sigma_{\Delta s}^2(\mathbf{r}) &= \left[ \frac{\partial \sigma_{\Delta \tau}^y(\mathbf{r})}{\partial x} \right]^2 + \left[ \frac{\partial \sigma_{\Delta \tau}^x(\mathbf{r})}{\partial y} \right]^2 + \left[ \frac{\sqrt{2} \sigma_{\Delta \tau}^x(\mathbf{r})}{L_y^x} \right]^2 \\ &\quad + \left[ \frac{\sqrt{2} \sigma_{\Delta \tau}^y(\mathbf{r})}{L_x^y} \right]^2, \end{aligned} \quad (34)$$

where  $L_y^x$  and  $L_x^y$  are the characteristic length scales (Daley 1991) defined as

$$L_y^x = \left( -\frac{2\rho_{\Delta \tau}^x}{\partial^2 \rho_{\Delta \tau}^x / \partial y^2} \right)^{1/2} \quad \text{and} \quad L_x^y = \left( -\frac{2\rho_{\Delta \tau}^y}{\partial^2 \rho_{\Delta \tau}^y / \partial x^2} \right)^{1/2}. \quad (35)$$

Equation (34) suggests that the total variance of  $\Delta \mathbf{s}$  depends on the characteristic length scales of the given wind stress error correlation functions. For simplicity, we represent the characteristic length scales in (34) by a single length scale  $L_S$ . At the limit  $L_S \rightarrow \infty$ , the third and fourth terms on the right-hand side of (34) vanish and the total variance is dominated by the shear of the wind stress error standard deviation. Inversely, at the limit  $L_S \rightarrow 0$ , the third and fourth terms become infinitely large and dominate the total variance. In an actual 4DVAR system, constructed on a finite number of grid points, these terms remain finite in the limit  $L_S \rightarrow \Delta r$ , where  $\Delta r$  is the horizontal grid size.

When  $\sigma_{\Delta \tau}^x$  and  $\sigma_{\Delta \tau}^y$  are functions of space and  $\Delta \hat{\tau}_x$  and  $\Delta \hat{\tau}_y$  are white noise processes in space, the cost function  $J_{\Delta \tau}$  in (19) can be written in the following form:

$$\begin{aligned} J_{\Delta \tau}[\Delta \tau_x, \Delta \tau_y] &= \frac{1}{2} \iint (\sigma_{\Delta \tau}^x)^{-2} (\Delta \tau_x \circ w_{\Delta \tau}^t \circ \Delta \tau_x) \, d\mathbf{r} \\ &\quad + \frac{1}{2} \iint (\sigma_{\Delta \tau}^y)^{-2} (\Delta \tau_y \circ w_{\Delta \tau}^t \circ \Delta \tau_y) \, d\mathbf{r}, \end{aligned} \quad (36)$$

where  $\circ$  is the inner product defined by

$$\alpha \circ \beta \equiv \iint \alpha(t) \beta(t) \, dt \quad (37)$$

and  $w_{\Delta \tau}^t$  is the weight function that satisfies

$$\rho_{\Delta \tau}^t(t_1; t_2) \circ w_{\Delta \tau}^t(t_1; t_2) = \delta(t_2 - t_1). \quad (38)$$

Special attention is required to derive the autocovariance function of the wind stress curl error inferred from the cost function in (36). Here  $\Delta \mathbf{s}_{\partial \sigma}$  can be defined as in the first part of (29) and its autocovariance function is derived from (32) by replacing  $\rho_{\Delta \tau}^{x(y)}$  with a delta function. Since  $\Delta \hat{\tau}_x$  and  $\Delta \hat{\tau}_y$  are uncorrelated white noise processes, the stochastic process  $\Delta \mathbf{s}_{\partial \sigma}$  is also a white noise process whose amplitude is modulated by shears of the wind stress error standard deviations. However, since  $\Delta \hat{\tau}_x$  and  $\Delta \hat{\tau}_y$  are not differentiable, we cannot formally define the autocovariance function of  $\Delta \mathbf{s}_{\partial \sigma}$ . In this case, it is useful to write the delta function as a limit of the Gaussian probability function:

$$\delta(\mathbf{r}) = \lim_{\epsilon \rightarrow 0} \delta_{\epsilon}(\mathbf{r}), \quad \delta_{\epsilon}(\mathbf{r}) \equiv \frac{1}{\epsilon \sqrt{\pi}} \exp\left(-\frac{|\mathbf{r}|^2}{\epsilon^2}\right). \quad (39)$$

Using this limit, the spatial correlation functions in (33) are approximated as

$$\begin{aligned}
 -\frac{\partial^2 \rho_{\Delta r}^y}{\partial \tilde{x}^2} &\cong \lim_{\epsilon \rightarrow \infty} \left[ \frac{2\sqrt{\pi}}{\epsilon} \left( 1 - \frac{2\tilde{x}^2}{\epsilon^2} \right) \right] \delta_\epsilon(\tilde{\mathbf{r}}) \quad \text{and} \\
 -\frac{\partial^2 \rho_{\Delta r}^x}{\partial \tilde{y}^2} &\cong \lim_{\epsilon \rightarrow \infty} \left[ \frac{2\sqrt{\pi}}{\epsilon} \left( 1 - \frac{2\tilde{y}^2}{\epsilon^2} \right) \right] \delta_\epsilon(\tilde{\mathbf{r}}). \quad (40)
 \end{aligned}$$

In a finite-difference scheme,  $\epsilon$  approaches  $\Delta r$ , but never 0.

In the foregoing discussion, it was shown that the wind stress error covariance function implicitly specifies the error covariance functions of the effective forcing for the wind-driven ocean circulation, namely, the wind stress curl error and wind stress divergence error. Furthermore, the relationship between the specific form of the cost function commonly used in 4D data assimilation and the implied wind stress curl error covariance was described. In the next section, we present numerical experiments designed to study a role of the wind stress curl error covariance function in shaping the a priori model error covariance matrix  $\mathbf{P}$ . Specifically, we investigate the impact of the wind stress curl error in the context of midlatitude, gyre-scale ocean circulation represented in a coarse-resolution OGCM.

#### 4. Design of numerical experiments

To set up our experiments, we use the primitive equation  $z$ -coordinate model (PEZ) developed at Oregon State University and its inverse modeling package with tangent linear and adjoint codes of PEZ (Chua and Bennett 2001; Muccino et al. 2008). The discretization scheme in PEZ is based on the Geophysical Fluid Dynamics Laboratory Modular Ocean Model, version 3.0 (MOM3; Pacanowski and Griffies 1999). The Richardson number-dependent vertical diffusivity and viscosity coefficients used in the original PEZ configuration are replaced by a simple Laplacian formulation with constant diffusivity and viscosity coefficients. The independent variables in our version of the PEZ model are the horizontal velocity components ( $u, v$ ), the free SSH  $\eta$ , and the potential density  $\rho_\theta$ . The baroclinic time step for the momentum and the potential density equations is 72 min, while the barotropic time step of 2 min is used to solve SSH explicitly. The model domain is shown in Fig. 1. It was designed so that it broadly resembles the Pacific basin over the latitudinal range of 20°S–60°N and longitudinal width of 100°. The horizontal grid size is 1.2° in both the zonal and meridional directions. The ocean bottom has been assigned a uniform depth of 4000 m and the vertical discretization has 20 levels with thicknesses ranging from 10 m at the top to 500 m near the bottom. The southern boundary at 20°S is assumed to be a rigid wall. Lateral boundary conditions were set to be no-slip in the momentum equations and no-flux in the potential density equation.

In the preliminary experiments, the horizontal eddy viscosity coefficient  $K_h$  was chosen from a range of values  $1.0 \times 10^4$ – $4.0 \times 10^4 \text{ m}^2 \text{ s}^{-1}$ , which are typical for coarse resolution ocean circulation models (e.g., Cox and Bryan 1984). Using various sizes of  $K_h$  within this range, we conducted data-less assimilation experiments (Bennett and Thorburn 1992; Ngodock et al. 2000) to test the stability of the tangent linear model without model error. Within this range, we chose a particular  $K_h$  value of  $4.0 \times 10^4 \text{ m}^2 \text{ s}^{-1}$ , for which the tangent linear solution of (6) converges to the nonlinear solution of (5) within a few Picard iterations over a 1-yr period. The vertical eddy viscosity coefficient  $K_v$ , horizontal eddy diffusivity coefficient  $A_h$  and vertical eddy diffusivity coefficient  $A_v$  were set to  $K_v = 1.0 \times 10^{-3} \text{ m}^2 \text{ s}^{-1}$ ,  $A_h = 1.0 \times 10^3 \text{ m}^2 \text{ s}^{-1}$ , and  $A_v = 3.0 \times 10^{-5} \text{ m}^2 \text{ s}^{-1}$ , respectively. Unstable vertical stratification was removed by applying the convective adjustment scheme (Cox 1984) to the water column wherever instability is detected. Because of the relatively coarse spatial resolution, there are no mesoscale eddies or baroclinic and barotropic instabilities in our model. Hence, dynamical balances in the large-scale ocean circulation are quasi-linear, except for the western boundary currents. The model ocean is driven at the surface by a buoyancy flux in the potential density equation and zonal wind stress forcing in the momentum equations. The buoyancy flux is determined by relaxing the sea surface potential density back to the zonally averaged annual climatology from the World Ocean Atlas 2001 (WOA; Conkright et al. 2002). The relaxation time scale was chosen to be 30 days. This buoyancy forcing is turned off after an initial 10-yr spinup run and before the following 1-yr experiments.

For simplicity, the known part of the wind stress forcing is specified as a zonal component that is steady and zonally uniform. The steady zonal wind stress was created by zonally averaging the Comprehensive Ocean–Atmosphere Data Set (COADS) climatological zonal wind stress (Trenberth et al. 1989) over the Pacific basin. The initial potential density was created by the zonally averaged WOA climatology for the Pacific basin. The ocean model was spun up from rest for 10 yr with the steady forcing fields and this provided a quasi-steady-state ocean circulation, as confirmed by total kinetic and potential energy calculations. The SSH at the end of the spinup run in Fig. 1 shows subtropical and subpolar gyres that are in reasonable agreement with characteristic dynamical circulation structures in the North Pacific Ocean. This result is used as the “perfect” initial condition for the calculation of the a priori model state error.

Two types of approximations are introduced in deriving the tangent linear model (TLM) and its adjoint model from the nonlinear forward model. The first

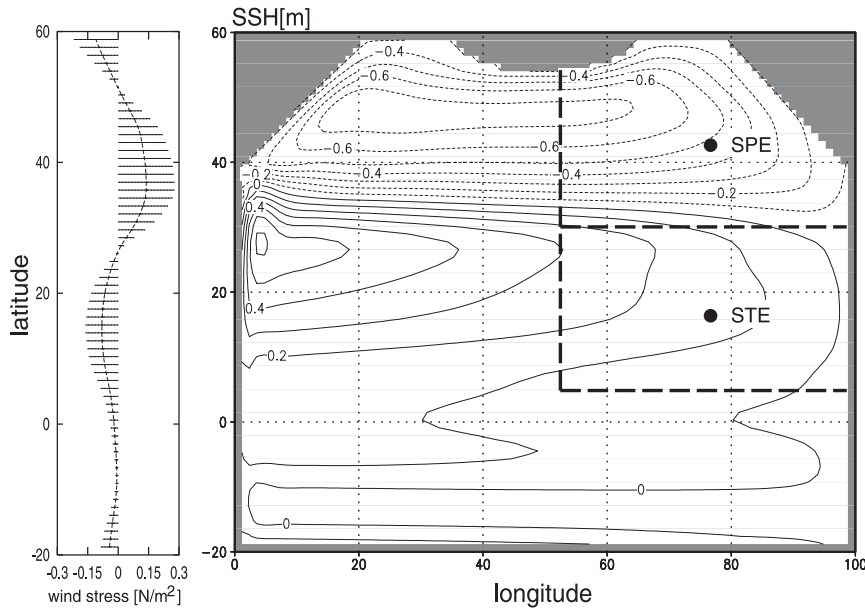


FIG. 1. Model configuration for the sensitivity experiments. (left) Zonal wind stress forcing (continuous line) and its std error (horizontal lines). (right) Model domain and mean sea level anomaly at the end of the spinup run (contours). The contour interval (CI) is 0.1 m. Two subdomains SPE and STE for subsequent statistical analysis are shown with dashed lines, and sample points for the calculation of the representer vector, SPE (42°N, 77°E) and STE (17°N, 77°E), are marked by black dots.

approximation is the elimination of the convective adjustment scheme in the tangent linear tracer equation (e.g., Weaver et al. 2003). Since the buoyancy flux is turned off after the spinup, the convective adjustment process is not active once a quasi-steady-state ocean circulation has been reached. This approximation was justified by preliminary experimental results showing that the root-mean-square (RMS) difference in SSH fields arising from the nonlinear model with and without the convective adjustment scheme remains in the order of  $10^{-6}$  cm for the 1-yr period after the spinup. The second approximation was introduced in order to reduce the storage size of the background model state vector, which is required by TLM and its adjoint model. We store the truncated background model state vector at every 20 baroclinic model time steps, which corresponds to one model day. The background model state vector is then reconstructed by interpolating the stored trajectory by using a step function. The RMS difference between the SSH outputs from the TLM with a truncated background model state vector and a full model state vector is on the order of  $10^{-3}$  cm over the same 1-yr period. Since the RMS errors are much smaller than the SSH standard deviation arising from the dynamical response to the wind stress error (on the order of a few centimeters), we conclude that both approximations have a minor impact on the structure of the a priori model state error. The

adjoint model is constructed based on the same approximations used for the TLM.

Based on the study of reanalysis wind datasets conducted by Gille (2005), we assume the following characteristics for the known and error components of wind stress forcing. (i) Zonally averaged climatological wind stress data are sufficiently precise that they may be used as known parts of the zonal wind stress forcing. (ii) The standard deviation of the zonal wind stress error is proportional to the mean zonal wind stress. For simplicity, it is also assumed that (iii) the zonal wind stress variance is zonally uniform and (iv) both the known and erroneous parts of the meridional wind stress forcing are zero. The resultant spatial structure of the zonal wind stress error variance then resembles the wind stress error variance used in previous ocean data assimilation studies (e.g., Stammer et al. 2002, 2003; Vialard et al. 2005).

Realizations of the zonal wind stress error  $\Delta\tau_x(\mathbf{r}, t)$  are simulated from the prescribed zonal wind stress error autocovariance function  $Q_{\Delta\tau}$ , assuming stationarity and uniformity of the stochastic process. We use the following form of  $Q_{\Delta\tau}$ :

$$Q_{\Delta\tau}(\mathbf{r}_1, t_1; \mathbf{r}_2, t_2) = \sigma_{\Delta\tau}(y_1)\rho(\tilde{x}, \tilde{y}, \tilde{t})\sigma_{\Delta\tau}(y_2), \quad (41)$$

where  $\tilde{x} \equiv x_2 - x_1$ ,  $\tilde{y} \equiv y_2 - y_1$ ,  $\tilde{t} \equiv t_2 - t_1$ ,  $\sigma_{\Delta\tau}$  is the zonal wind stress error standard deviation, and  $\rho_{\Delta\tau}$  is the

normalized wind stress error autocorrelation function. In this experiment,  $\sigma_{\Delta\tau}$  is chosen to be  $\sigma_{\Delta\tau}(y) = |\bar{\tau}_x(y)|$ , where  $\bar{\tau}_x(y)$  is the steady zonal wind stress defined from the climatology (see the left panel in Fig. 1 and Fig. 10a). Here  $\rho_{\Delta\tau}$  is assumed to be homogeneous and separable in all coordinate directions as

$$\rho_{\Delta\tau}(\tilde{x}, \tilde{y}, \tilde{t}) = \exp\left(-\frac{\tilde{x}^2}{L_X^2}\right) \exp\left(-\frac{\tilde{y}^2}{L_Y^2}\right) \exp\left(-\frac{|\tilde{t}|}{L_T}\right), \quad (42)$$

where  $L_X$ ,  $L_Y$ , and  $L_T$  are decorrelation scales in the zonal, meridional, and temporal coordinates, respectively. The convolution between the correlation function in (42) and the adjoint variables is performed by a diffusion equation for the spatial correlation and the Langevin equation for the temporal correlation (Chua and Bennett 2001; Bennett 2002). The function form for (42) is chosen to reproduce two cases: (i) a diagonal covariance matrix (e.g., Stammer et al. 2002) and (ii) a nondiagonal covariance matrix based on the wind stress covariance of reanalysis data (e.g., Fukumori et al. 1999). Case i is represented by choosing the decorrelation length scales  $L_X$ ,  $L_Y$ , and time scale  $L_T$  of the same order as the horizontal model grid resolution and time step size. Case ii is represented by choosing decorrelation length and time scales corresponding to reanalysis data. Although it is not in the scope of this study, it should be noted that the error covariance structure inferred from a difference between the power spectra of reanalysis wind stress data and satellite-derived data

(Milliff et al. 2004; Gille 2005) does not support any of these structures. Rather, a plausible wind stress error covariance has more power in higher wavenumbers and frequencies.

The wind stress curl error  $\Delta\varsigma$  is derived from (28), (29), and (34) as

$$\Delta\varsigma(x, y) = -\frac{\partial\sigma_{\Delta\tau}(y)}{\partial y} \Delta\hat{\tau}_x(x, y) - \frac{\sqrt{2}\sigma_{\Delta\tau}(y)}{L_Y} \Delta\hat{\varsigma}(x, y), \quad (43)$$

where we assume that  $\Delta\tau_y = 0$ . Here  $\Delta\varsigma$  consists of two stochastic variables, the normalized zonal wind stress error  $\Delta\hat{\tau}_x$  and the normalized wind stress curl error  $\Delta\hat{\varsigma} \equiv (\partial\Delta\hat{\tau}_x/\partial y)(L_Y/\sqrt{2})$ . The variance of  $\Delta\varsigma$  is then given by

$$\sigma_{\Delta\varsigma}^2(y) = \left[\frac{\partial\sigma_{\Delta\tau}(y)}{\partial y}\right]^2 + \frac{2}{L_Y^2} \sigma_{\Delta\tau}^2(y). \quad (44)$$

Equations (44) is consistent with the general expression in (34). The variance of the first term on the right-hand side of (44) is given by the meridional gradient of the originally specified zonal wind stress error standard deviation. The variance of the second term is a product of the variance of the zonal wind stress error and  $2L_Y^{-2}$ . Thus, the variance of the first term has a smaller spatial scale than the second term and its peaks appear where the meridional gradient of the zonal wind stress error standard deviation are at local maxima. The autocovariance function of  $\Delta\varsigma$  is then written as

$$\begin{aligned} Q_{\Delta\varsigma\Delta\varsigma}(\mathbf{r}_1, t_1; \mathbf{r}_2, t_2) &= \frac{\partial\sigma_{\Delta\tau}(y_1)}{\partial y} \rho_{\Delta\tau}(\tilde{x}, \tilde{y}, \tilde{t}) \frac{\partial\sigma_{\Delta\tau}(y_2)}{\partial y} + \frac{\sqrt{2}\sigma_{\Delta\tau}(y_1)}{L_Y} \rho_{\Delta\hat{\varsigma}}(\tilde{x}, \tilde{y}, \tilde{t}) \frac{\sqrt{2}\sigma_{\Delta\tau}(y_2)}{L_Y} \\ &\quad - \frac{\sqrt{2}}{L_Y} \left[ \frac{\partial\sigma_{\Delta\tau}(y_1)}{\partial y} \right] \rho_{\Delta\hat{\varsigma}\Delta\hat{\tau}}(\tilde{x}, \tilde{y}, \tilde{t}) \left[ \sigma_{\Delta\tau}(y_2) \frac{\partial\sigma_{\Delta\tau}(y_2)}{\partial y} \right] \frac{\sqrt{2}}{L_Y}, \end{aligned} \quad (45)$$

where  $\rho_{\Delta\tau}$  is the autocovariance function of  $\Delta\hat{\tau}_x$  of the form (42). The autocovariance function of  $\Delta\hat{\varsigma}$  and the cross covariance between  $\Delta\hat{\varsigma}$  and  $\Delta\hat{\tau}_x$  have the following form:

$$\rho_{\Delta\hat{\varsigma}}(\tilde{x}, \tilde{y}, \tilde{t}) = \left(1 - \frac{2}{L_Y^2} \tilde{y}^2\right) \rho_{\Delta\tau}(\tilde{x}, \tilde{y}, \tilde{t}) \quad \text{and} \quad (46)$$

$$\rho_{\Delta\hat{\varsigma}\Delta\hat{\tau}}(\tilde{x}, \tilde{y}, \tilde{t}) = \tilde{y} \rho_{\Delta\tau}(\tilde{x}, \tilde{y}, \tilde{t}). \quad (47)$$

The power spectral density functions (PSDs) of the two stochastic processes  $\Delta\hat{\tau}_x$  and  $\Delta\hat{\varsigma}$  are derived from (42) and (46), respectively, as

$$\begin{aligned} h_{\Delta\hat{\tau}}(k, l, \omega) &= \frac{L_X}{\sqrt{2}} \exp\left(-\frac{L_X^2}{4} k^2\right) \frac{L_Y}{\sqrt{2}} \exp\left(-\frac{L_Y^2}{4} l^2\right) \\ &\quad \times \sqrt{\frac{2}{\pi}} \frac{L_T}{1 + L_T^2 \omega^2} \quad \text{and} \end{aligned} \quad (48)$$

$$h_{\Delta\hat{\varsigma}}(k, l, \omega) = \left(\frac{L_Y}{\sqrt{2}} l\right)^2 h_{\Delta\hat{\tau}}(k, l, \omega), \quad (49)$$

where  $(k, l)$  are the horizontal wavenumbers of the zonal and meridional components, and  $\omega$  is the angular frequency.

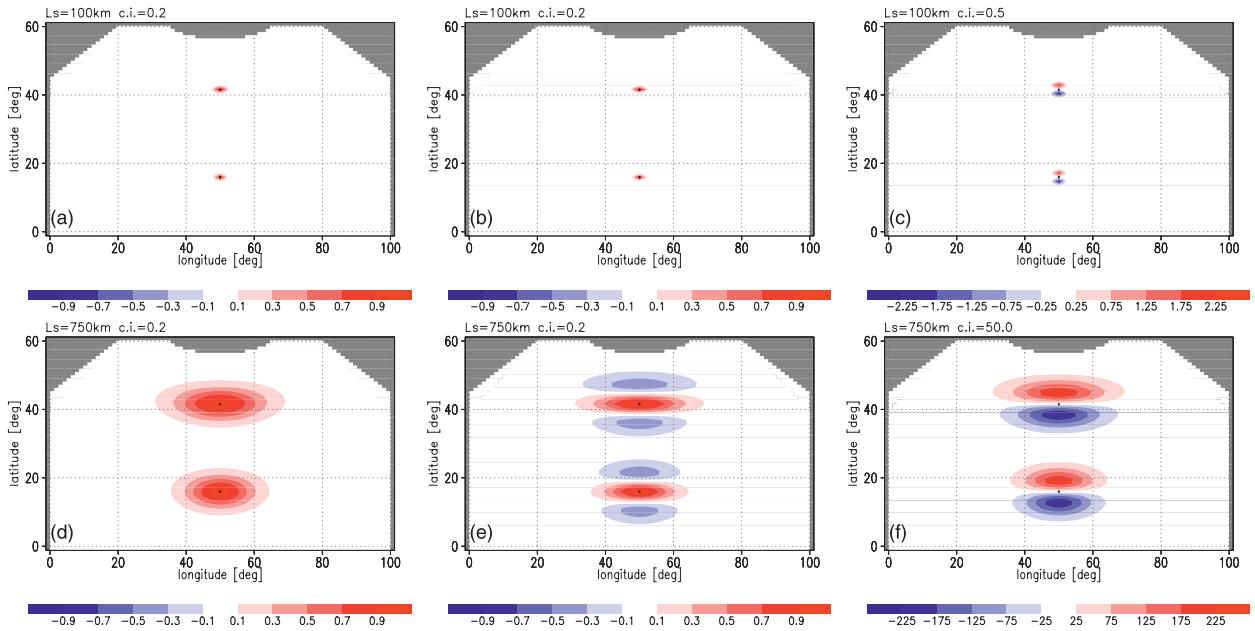


FIG. 2. Spatial structure of the correlation functions in (45) for (top)  $L_S = 100$  km and (bottom)  $L_S = 750$  km. Correlation functions are computed at STE ( $17^\circ\text{N}$ ,  $50^\circ\text{E}$ ) and at SPE ( $42^\circ\text{N}$ ,  $50^\circ\text{E}$ ), marked by black dots. Autocorrelation function of (a),(d) normalized wind stress error,  $\rho_{\Delta\tau}$ , and (b),(e) normalized wind stress curl error,  $\rho_{\Delta\hat{s}}$ . (c),(f) The cross-correlation function of normalized wind stress curl and normalized wind stress error,  $\rho_{\Delta\hat{s}\Delta\tau}$ . The CI is 0.2, but is 0.5 in (c) and 50 in (f).

To reduce the number of independent parameters in the error correlation function, we constrain the ratio of the zonal decorrelation length scale  $L_X$  to the meridional decorrelation length scale  $L_Y$  as  $L_X:L_Y = 1:2$  and introduce a mean decorrelation length scale of  $L_S = (L_X + L_Y)/2$ . The adjustable parameters in the wind stress error correlation function are then  $L_S$  and  $L_T$  in the following experiments.

The  $L_S$  of the zonal wind stress error covariance is set to 100 and 750 km in these experiments. The  $L_S = 100$ -km case corresponds to the case i of the diagonal covariance matrix in spatial coordinates. For the case ii,  $L_S = 750$  km is determined from the PSD of the National Centers for Environmental Prediction (NCEP) analysis (Milliff et al. 2004). The spatial structure of the correlation functions in (42), (46), and (47) are plotted in Fig. 2 for the two decorrelation length scales. For  $L_S = 100$  km, the spatial structure of the correlation function in (46) is not distinguishable from the structure of (42) with a single peak at its center. For  $L_S = 750$  km, the correlation function of  $\Delta\hat{s}$  is seen to have one positive peak at its center and two negative peaks: one to the north and one to the south. For both cases, the spatial structure of cross-correlation function in (47) is characterized by two peaks with one negative peak south of center and one positive peak to the north. As discussed later, the distinct spatial structures of these correlation functions are good indicators for checking the influence of each

term on the right-hand side of (45) on the shape of  $\tilde{\mathbf{P}}$ . Two decorrelation time scales,  $L_T = 1$  day and  $L_T = 10$  days are also chosen. The former corresponds to the case of a diagonal matrix in temporal coordinates while the latter is determined from the frequency spectra of reanalysis wind stress products (Gille 2005). The resultant PSDs of the autocorrelation functions, (48) and (49), are plotted in Fig. 3. Since the frequency and zonal wavenumber spectra in Figs. 3a,b are common in both PSDs, it is the meridional wavenumber spectra that differs between the two stochastic processes  $\Delta\hat{\tau}$  and  $\Delta\hat{s}$ . The major difference between the two meridional wavenumber spectra is that the spectra of  $\Delta\hat{s}$  has a high peak at the characteristic wavenumber  $l_c = 2/L_Y$  whereas the spectra of the wind stress error are flat below  $l_c$  and descend beyond  $l_c$ .

The representer vector  $\mathbf{p}_m^{\eta}$  is computed by the ensemble solution in (13), based on 100 realizations of the model state vector that were produced by perturbing the OGCM with wind stress errors that obey the error covariance functions in (41) and (42). Realizations of the wind stress error were generated using a diffusion equation in space and a first-order autoregression model in time (Bennett 2002). The vector  $\mathbf{p}_m^{\eta}$  is also computed by solving (14). We chose the two spatial locations SPE (at  $42^\circ\text{N}$ ,  $77^\circ\text{E}$ ) and STE (at  $17^\circ\text{N}$ ,  $77^\circ\text{E}$ ) in Fig. 1 as sample locations and day 360 as a sample time to compute  $\mathbf{p}_m^{\eta}$ . Since  $\mathbf{p}_m^{\eta}$  has the length of the model state

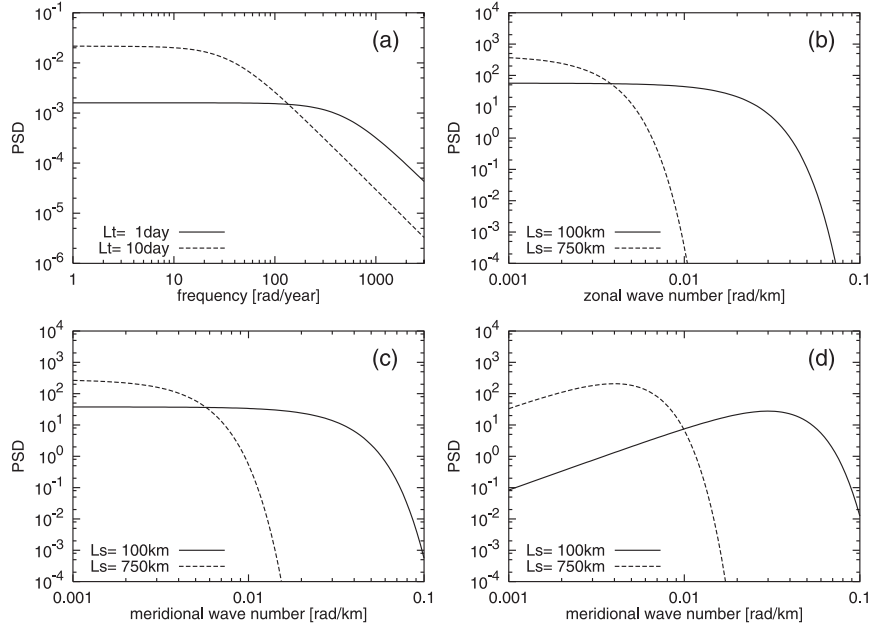


FIG. 3. Power spectral density function of correlation functions in (42), (46), and (47) for the normalized zonal wind stress error and the normalized wind stress curl error. (a) Frequency spectra for wind stress and wind stress curl errors. (b) Zonal wavenumber spectra for the wind stress and wind stress curl errors. (c) Meridional wavenumber spectra for the wind stress error. (d) Meridional wavenumber spectra for the wind stress curl error. Frequency spectra are computed for two decorrelation time scales,  $L_T = 1$  day and  $L_T = 10$  days in (a). The wavenumber spectra are computed for two decorrelation length scales,  $L_S = 100$  km and  $L_S = 750$  km in (b), (c), and (d).

vector  $\mathbf{x}$  in the four-dimensional space of the OGCM, the vector  $\mathbf{p}_m^\eta$  is still too large to summarize the dependencies of  $\mathbf{P}$  to  $\mathbf{Q}$ . Here, we define a further-truncated subspace of  $\hat{\mathbf{P}}$  as

$$\hat{\mathbf{p}}_m^\eta \equiv \sigma_\eta^{-1}(\mathbf{r}_m, t_m) \mathbf{H}_m^\eta \mathbf{p}_m^\eta, \tag{50}$$

where  $\sigma_\eta^2(\mathbf{r}_m, t_m) \equiv \langle [\eta(\mathbf{r}_m, t_m) - \langle \eta(\mathbf{r}_m, t_m) \rangle]^2 \rangle$  and  $\mathbf{H}_m^\eta$  is the matrix that projects  $\mathbf{x}$  onto the SSH at the sample time  $t_m$ . Hereafter, we call the column vector  $\hat{\mathbf{p}}_m^\eta$  a normalized representer vector. From the definition of  $\mathbf{p}_m^\eta$  in (13),  $\hat{\mathbf{p}}_m^\eta$  can also be calculated from

$$\hat{\mathbf{p}}_m^\eta \equiv \sigma_\eta^{-2}(\mathbf{r}_m, t_m) \langle [\eta(\mathbf{r}, t_m) - \langle \eta(\mathbf{r}, t_m) \rangle] [\eta(\mathbf{r}_m, t_m) - \langle \eta(\mathbf{r}_m, t_m) \rangle] \rangle. \tag{51}$$

The vectors  $\hat{\mathbf{p}}_m^\eta$  are calculated for the selected sample points from (50) and (51) for cross-validation purposes. The integration period is set to 1 yr for all experiments.

### 5. Results of numerical experiments and discussion

Figure 4 shows a vector  $\hat{\mathbf{p}}_m^\eta$  computed by the two methods for the sample locations SPE and STE at the

sample time  $t_m = \text{day } 30$ . In these experiments, the decorrelation length scale of the wind stress error covariance is set to  $L_S = 100$  km and  $L_S = 750$  km and the time scale is set to  $L_T = 10$  days. Here  $\hat{\mathbf{p}}_m^\eta$  obtained by the ensemble method in (51) is generally contaminated by noise because of the limited number of ensemble members, as shown in Figs. 4a,b. However, the two solutions around the sample point (black dot in the figures), calculated by the two methods, show good agreement. The same level of agreement can be found at  $t_m = \text{day } 360$ . For the case  $L_T = 1$  day, solutions obtained with the direct representer method in (50) have a tendency to be numerically unstable for both  $L_S = 100$  km and  $L_S = 750$  km (not shown here). This error occurs only when the temporal correlation matrix is chosen to be diagonal in the direct representer method and does not influence to the other solutions in this study. Since the ensemble method produced a numerically stable solution within the ranges of  $L_S$  and  $L_T$  used in this study, we focus on the solutions obtained from (51) in subsequent discussions.

At both sample locations SPE and STE, the spatial structure of  $\hat{\mathbf{p}}_m^\eta$  does not change significantly as a function of the sample time  $t_m$ , but its amplitude, namely the

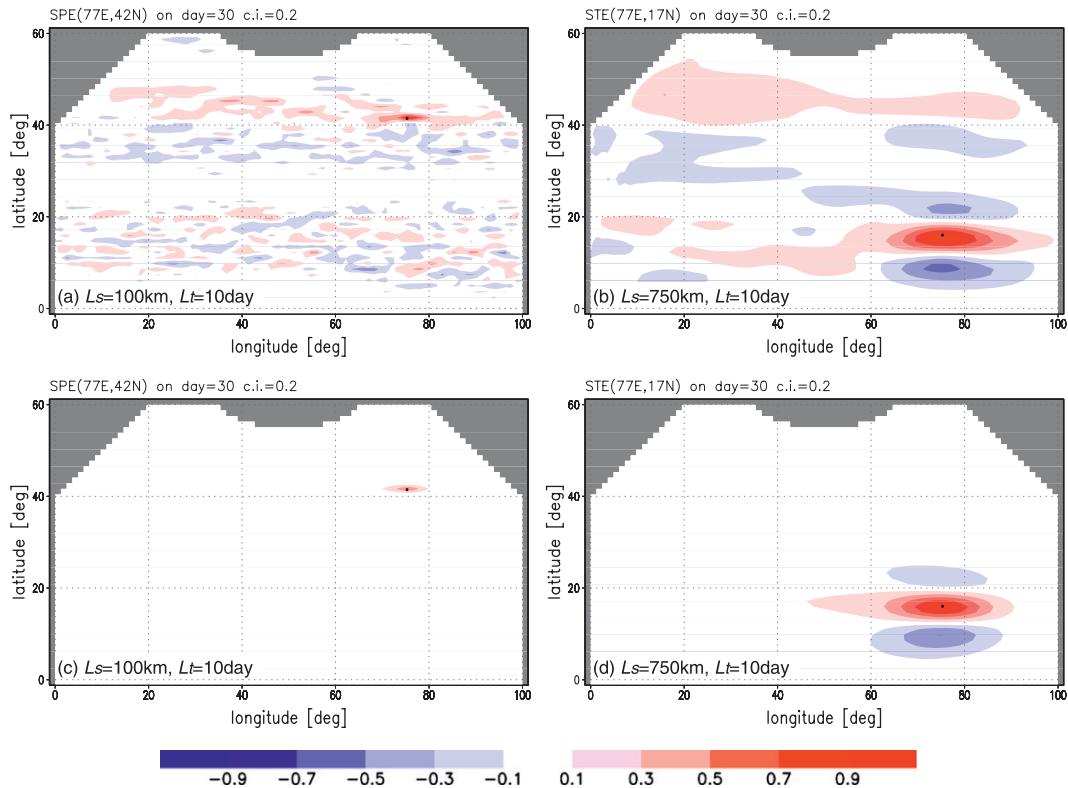


FIG. 4. Comparison of the normalized representer vectors calculated by the (top) ensemble method and (bottom) the direct representer method. Representer vectors are computed for the sea surface measurement at points SPE (42°N, 77°E) and STE (17°N, 77°E), marked by black dots, with a 1-month integration period. (a),(c) Solutions for the wind stress error with  $L_S = 100$  km and  $L_T = 10$  days, respectively. (b),(d) Solutions for  $L_S = 750$  km and  $L_T = 10$  days, respectively. The CI is 0.2.

SSH error variance at the sample location,  $\sigma_{\eta}^2(\mathbf{r}_m, t_m)$ , changes through the range of  $t_m$ . To smooth out the shorter scale noise due to the limited number of ensembles in a plot of  $\sigma_{\eta}^2(\mathbf{r}_m, t_m)$  (not shown here), we averaged  $\sigma_{\eta}^2(\mathbf{r}_m, t_m)$  over the subdomain that surrounds each sample location (Fig. 1). The time series of averaged SSH error variance,  $\bar{\sigma}_{\eta}^2(\mathbf{r}_m, t_m)$ , at domains SPE and STE are shown in Fig. 5. In both domains,  $\bar{\sigma}_{\eta}^2(\mathbf{r}_m, t_m)$  grows continuously. Its amplitude is smaller when  $L_S$  or  $L_T$  is shorter. The sensitivity of  $\bar{\sigma}_{\eta}^2(\mathbf{r}_m, t_m)$  to a change in the size of  $L_S$  is higher for  $L_T = 10$  days than for  $L_T = 1$  day. The rate of change in  $\bar{\sigma}_{\eta}^2(\mathbf{r}_m, t_m)$  as  $L_S$  increases from 100 to 750 km is about 30% at domain SPE (Fig. 5a) while the change in  $\bar{\sigma}_{\eta}^2(\mathbf{r}_m, t_m)$  is about 11% at domain STE (Fig. 5c) when  $L_T$  is set to 1 day. When  $L_T$  is set to 10 days, the rate of change in  $\bar{\sigma}_{\eta}^2(\mathbf{r}_m, t_m)$  as  $L_T$  increased was about 100% in both domains (Figs. 6b,d).

Figure 6 shows the spatial structure of  $\hat{\mathbf{p}}_m^{\eta}$  for  $L_S = 100$  km at  $t_m = \text{day } 360$ . Each panel shows a single positive peak at  $\mathbf{r}_m$  and the length scale of  $\hat{\mathbf{p}}_m^{\eta}$  is close to the length scale of the wind stress curl error correlation

shown in Figs. 2a,b. The influence of the cross-correlation term in the wind stress curl error cannot be observed. When  $L_S$  is increased to 750 km, the spatial structure of  $\hat{\mathbf{p}}_m^{\eta}$  (Fig. 7) also has the same order of length scale as the wind stress curl error covariance functions in Figs. 2d,e. Again, the influence of the cross-correlation term in the wind stress curl error cannot be observed. The similarity of the covariance function structures between the wind stress curl error and the SSH error indicates that the model state error is due to a local response of ocean dynamics to the wind stress curl error.

Contrary to the case where  $L_S$  is set to 100 km, the spatial structure of  $\hat{\mathbf{p}}_m^{\eta}$  shows dependencies on the size of  $L_T$  and the latitude of  $\mathbf{r}_m$  when  $L_S$  is set to 750 km. For  $L_T = 1$  day, the spatial pattern of  $\hat{\mathbf{p}}_m^{\eta}$  in Figs. 7a,c is dominated by a single positive peak around  $\mathbf{r}_m$ . This pattern resembles the characteristic spatial structure of the first term of the wind stress curl error correlation function in (45) in Fig. 2d. This resemblance indicates that the model state error is mainly controlled by a local response of the ocean dynamics to the first term of the wind stress curl error in (43). The influence of the

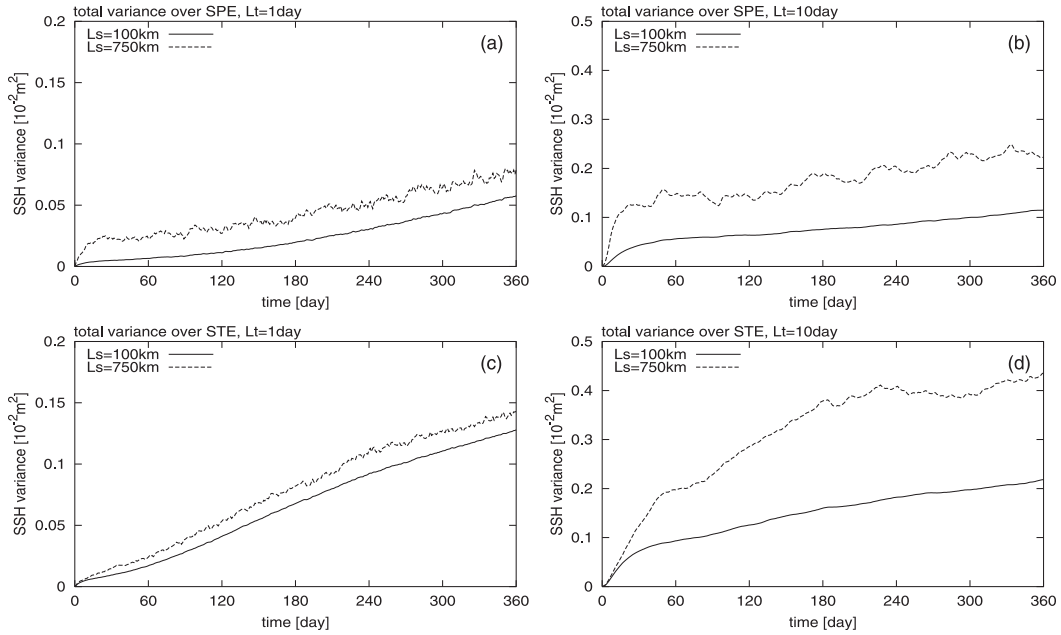


FIG. 5. Time series of SSH error variance averaged over the subdomains (a),(b) SPE and (c),(d) STE defined in Fig. 1. The decorrelation length scale of wind stress error covariance is chosen to be  $L_S = 100$  km (continuous line) and  $L_S = 750$  km (dashed line). (a),(c) Computed from a 100-member ensemble of SSH errors for  $L_T = 1$  day and (b),(d) are for  $L_T = 10$  days.

second term in (43) on  $\hat{\mathbf{p}}_m^\eta$  is clearer when  $L_T$  is set to 10 days, as shown in Figs. 7b,d. At the sample location SPE,  $\hat{\mathbf{p}}_m^\eta$  has a positive peak around the sample location and two negative peaks to the north and the south (Fig. 7b). The pattern resembles the characteristic structure of the wind stress curl error correlation function in (46) in Fig. 2e. At STE (Fig. 7d), the negative peak to the north of the positive peak is not seen as it was in Fig. 4d. However, the northern negative peak is clearly seen in the direct representer solution of  $\hat{\mathbf{p}}_m^\eta$  (not shown here), which is similar to the solution at  $t_m = \text{day } 30$  (Fig. 4d). We conclude that the spatial pattern found in Fig. 7d is also determined by the ocean response to the second term of the wind stress curl error in (43).

In Fig. 7b,  $\hat{\mathbf{p}}_m^\eta$  is elongated to the west away from the sample point SPE. Thus, the model response to the wind stress curl error is both local and remote. The zonally elongated structure can be obtained at a sample time as early as  $t_m = \text{day } 20$ . Considering the relatively short time scale for the SSH error correlation to reach to the western boundary, the structure is likely due to the response of the barotropic Rossby wave to the stochastic wind stress curl (Willebrand et al. 1980). To examine the degree of contribution from barotropic dynamics to  $\hat{\mathbf{p}}_m^\eta$ , we computed another set of vectors  $\hat{\mathbf{p}}_m^\eta$  for the barotropic OGCM with the same set of error covariance parameters,  $L_S$  and  $L_T$ . The barotropic OGCM has exactly the same configuration as that of the OGCM

described in section 4, except for an initially uniform potential density.

The two panels in Fig. 8 show the vector  $\hat{\mathbf{p}}_m^\eta$  from the barotropic experiments at the sample point SPE. When  $L_T$  is set to 1 day (Fig. 8a),  $\hat{\mathbf{p}}_m^\eta$  has a spatial structure similar to that of the first term of the wind stress curl error correlation function in (42) (Fig. 2d). Thus, the barotropic response of the model state error is also local to the wind stress curl error. The locality of the barotropic response to the wind stress disturbance with a time scale as short as 1 day is discussed in Willebrand et al. (1980) and our result is consistent with their analysis. For  $L_T = 10$  days,  $\hat{\mathbf{p}}_m^\eta$  shows a zonally elongated structure similar to that observed in Fig. 7b. Thus, we can infer that the westward elongation of  $\hat{\mathbf{p}}_m^\eta$  at the sample location SPE is due to the barotropic response of the model dynamics.

The time series of  $\bar{\sigma}_\eta^2(t)$  from the barotropic experiments are plotted in Fig. 9, analogous to Fig. 5. The barotropic SSH error variance is negligibly small over the subdomain SPE when  $L_S$  is set to 100 km (Figs. 9a,b) compared to the total variance (Figs. 5a,b). The barotropic SSH error variances over the subdomain STE are also negligibly small when  $L_T$  is set to either 1 or 10 days (Figs. 9c,d) compared to the total variance (Figs. 5c,d). However, the amplitude of  $\bar{\sigma}_\eta^2(t)$  over the subdomain SPE when  $L_S = 750$  km (Figs. 9a,b) is comparable to that of the original variance (Figs. 5a,b).

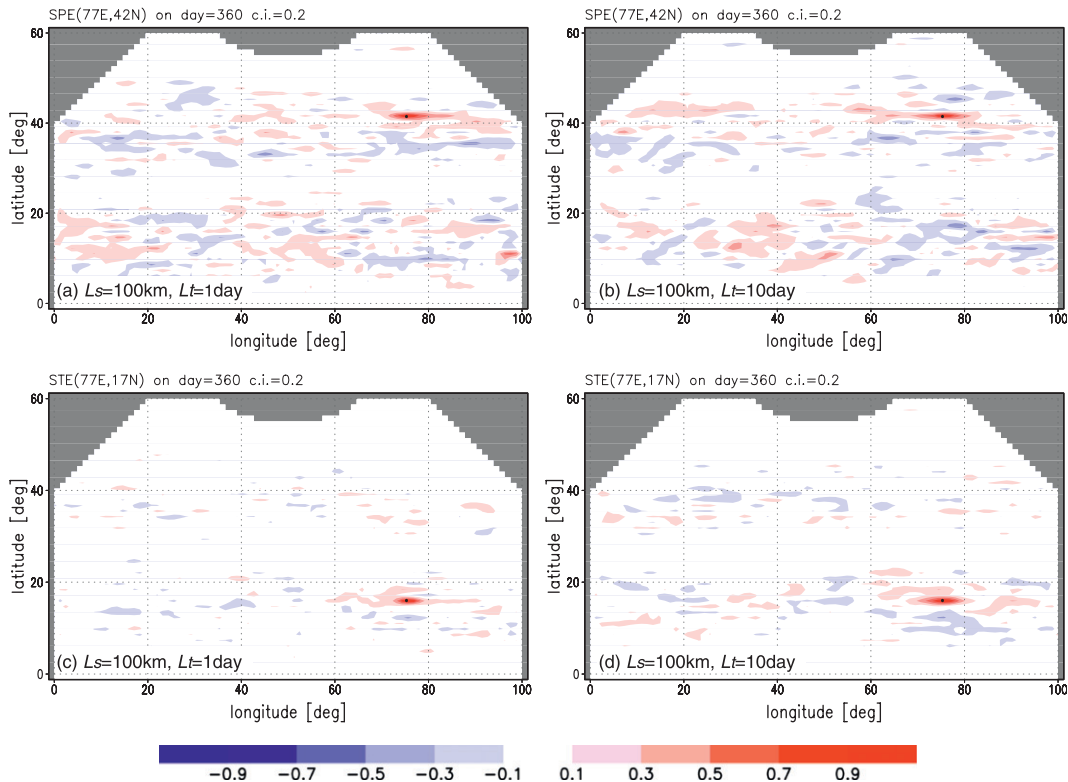


FIG. 6. Spatial structure of the normalized representer vectors projected on SSH and computed at the two locations (top) SPE (42°N, 77°E) and (bottom) STE (17°N, 77°E) at day 360. The decorrelation time scale of the wind stress error covariance is chosen to be (a),(c)  $L_T = 1$  day and (b),(d)  $L_T = 10$  days. The decorrelation length scale  $L_S = 100$  km is used for all cases. The CI is 0.2.

In the subpolar gyre, the level of the SSH error variance  $\bar{\sigma}_\eta^2(t)$  changes by about  $0.4 \times 10^{-3} \text{ m}^2$  for  $L_T = 1$  day (Fig. 5a) and about  $1.0 \times 10^{-3} \text{ m}^2$  for  $L_T = 10$  day (Fig. 5b) when the decorrelation length scale in the wind stress error changes from  $L_S = 100$  km to  $L_S = 750$  km. The same order of changes in the SSH error variance can be found in the barotropic experiments (Figs. 9a,b). Furthermore, the fluctuations in the time series of  $\bar{\sigma}_\eta^2(t)$  for  $L_S = 750$  km have a similar structure in both the baroclinic and barotropic experiments. These results indicate that the sensitivity of the SSH error variance to a change in  $L_S$  at the subpolar gyre is mainly explained by the barotropic response and that the baroclinic and the barotropic responses are independent stochastic processes. In the subtropical gyre, the sensitivity of the SSH error variance to changes in  $L_S$  (Figs. 5c,d) can be explained by the baroclinic response (Figs. 5c,d), not the barotropic.

The time series of  $\bar{\sigma}_\eta^2(\mathbf{r}_m, t_m)$  in the barotropic experiments (Fig. 9) reaches a quasi-steady state in about 20 days, near the time when the zonally elongated pattern of  $\hat{\mathbf{p}}_m^\eta$  emerges (Fig. 8b). On the other hand,  $\bar{\sigma}_\eta^2(\mathbf{r}_m, t_m)$  in the original experiments increases steadily over the 1-yr period (Fig. 5). Thus, the relative contri-

bution from the barotropic response to  $\hat{\mathbf{P}}$  becomes smaller as the perturbation period becomes longer. The progressive change of the dynamical balance in  $\hat{\mathbf{P}}$  is due to the growing baroclinic response to the wind stress curl error. Considering a propagation speed of the baroclinic Rossby wave, it may take an extra 10 yr for  $\hat{\mathbf{P}}$  to reach a steady state. The difference in the equilibrium time scale between the barotropic response and baroclinic response indicates that the dynamical balance in  $\hat{\mathbf{P}}$ , shaped by the wind stress error, keeps changing during the perturbation period of 1 yr.

The shift in the dominant forcing term for  $\hat{\mathbf{P}}$  with changing  $L_T$  (see Fig. 7) can also be observed in the spatial structure of the SSH error variance,  $\sigma_\eta^2$ . Figures 10 b,c show the meridional distribution of  $\sigma_\eta^2$  at day 360. Here  $\sigma_\eta^2$  is zonally averaged to remove small-scale noise. When  $L_T$  is set to 1 day,  $\sigma_\eta^2$  shows the three peaks at around 12°, 23°, and 28°N for both decorrelation length scales. The first peak is attributed to the peak of  $\sigma_{\Delta\tau}^2(y)$  at around 14°N in Fig. 10a and the second and the third peaks are attributed to the peaks of  $[\partial\sigma_{\Delta\tau}(y)/\partial y]^2$  at around 24° and 28°N. The other peaks in the wind stress curl error variance at higher latitudes do not appear in

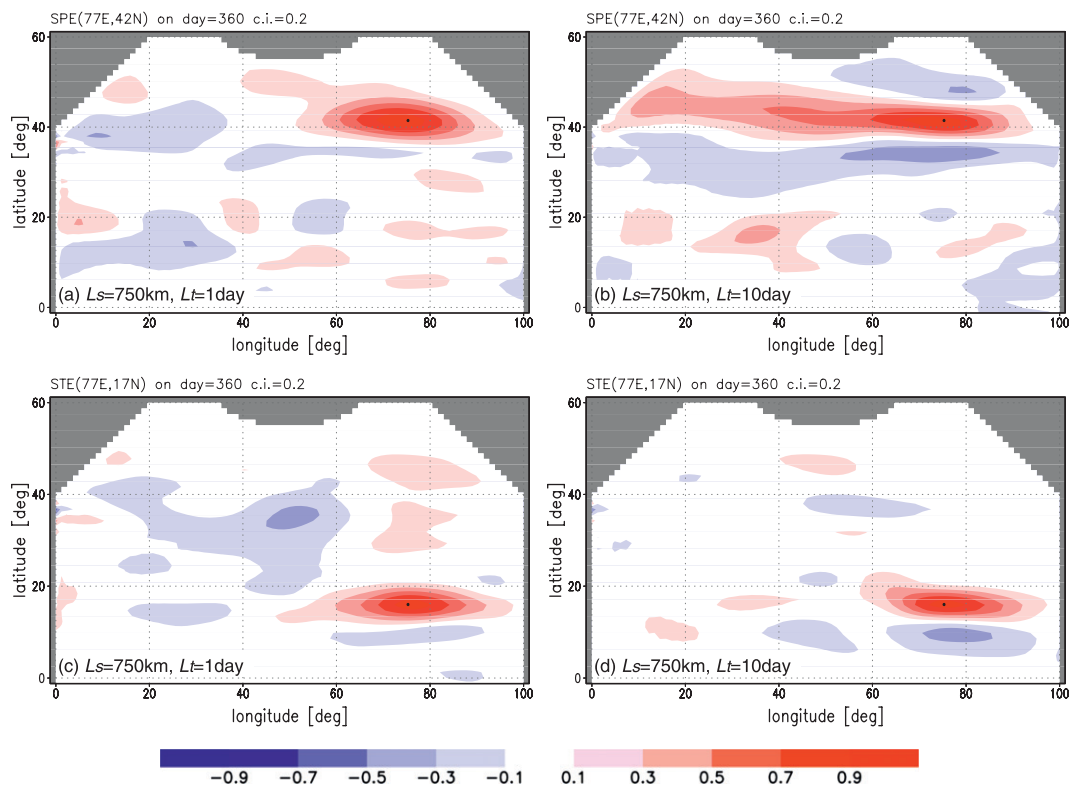


FIG. 7. As in Fig. 6, but the decorrelation length scale is now  $L_S = 750$  km.

the SSH error variance. On the other hand, when  $L_T$  is set to 10 days, the wind stress curl error shows an influence on the SSH error variances at higher latitudes. With this time scale, the  $\sigma_\eta^2$  also starts to show high sensitivity to the size of  $L_S$ . The three peaks for  $L_S = 100$  km in Fig. 10c are at the same latitudes as the three peaks in Fig. 10b. When  $L_S$  is set to 750 km, the three peaks are still recognizable in  $\sigma_\eta^2$  (Fig. 10c). Differences from the case of  $L_S = 100$  km are the dominance of the first peak over the other peaks and the newly appearing fourth peak around 38°N. The fourth peak can be attributed to the peak in  $\sigma_{\Delta\tau}^2(y)$  at around 36°N in Fig. 10a. Since the two peaks at around 14° and 38°N in Fig. 7c for  $L_S = 750$  km are both attributed to the peaks of  $\sigma_{\Delta\tau}^2(y)$ , their amplification with the increase of  $L_S$  from 100 to 750 km can be explained by the strengthening of the influence of the second term in the wind stress curl error in (43).

Although the dynamical reason for this shift in the effective forcing term in the wind stress curl error is not clear, its impact on the 4DVAR analysis would be significant. If all the measurements in the optimal solutions in (11) and (3) are made on SSH, then the representer matrix  $\tilde{\mathbf{S}}$  is equal to the covariance matrix of the a priori SSH error at the measurement points. The SSH error variance in Fig. 10 corresponds to the diagonal com-

ponents of  $\tilde{\mathbf{S}}$ . The role of the matrix  $\tilde{\mathbf{S}}$  in (11) is to determine the relative importance of each model–data misfit in the innovation vector  $\mathbf{d}$  together with a measurement error matrix  $\mathbf{R}$ . The larger the size of the error variance, the larger the contribution that the model–data misfit at the sample point makes to the optimal solution. In our case, when  $L_T$  is set to 10 days, the optimal solution for the SSH measurement is anticipated to change significantly, depending on the choice of  $L_S$ .

### 6. Conclusions

The role of the random component of the wind stress error in the 4DVAR data assimilation system of a basin-scale, midlatitude ocean circulation model has been investigated. It was shown that the wind stress error covariance functions, when expressed in terms of zonal and meridional wind stress errors, implicitly specify the error covariance functions of the effective forcing errors, which are the wind stress curl error and the wind stress divergence error. The wind stress curl error covariance was derived for a given wind stress error covariance function of the Gaussian type. The impact of the wind stress curl error covariance on the shape of the a priori model state error covariance matrix  $\mathbf{P}$ , which is approximated by  $\tilde{\mathbf{P}}$ , was examined.

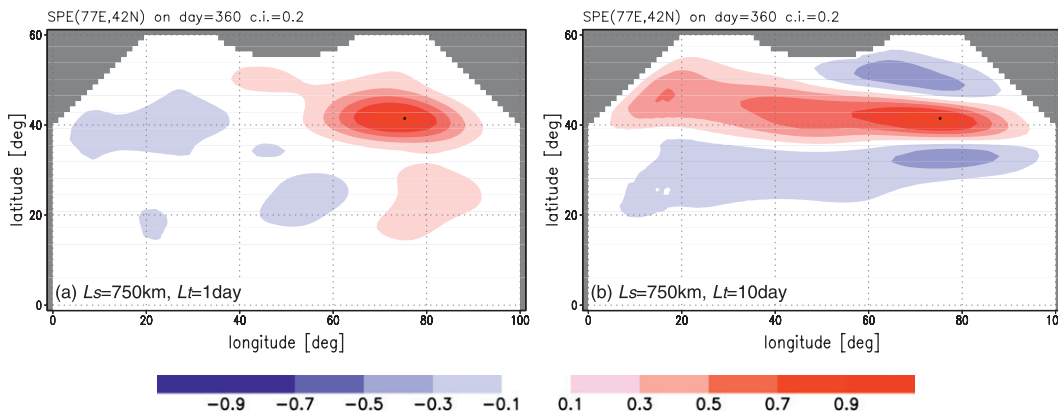


FIG. 8. Normalized representer vectors computed by the barotropic model for the decorrelation length scale  $L_S = 750$  km and time scales (a)  $L_T = 1$  day and (b)  $L_T = 10$  days.

Our experiments show that the wind stress curl error covariance, determined by a wind stress error covariance, has a strong impact on the shape of  $\mathbf{P}$ . However, in a standard 4DVAR ocean data assimilation system, the wind stress curl error covariance is generally not directly specified. The responses of the model state error to a wind stress curl error are mainly characterized by two dynamical responses at the exact location of the forcing. One is the local response in both baroclinic and barotropic modes, which project the model–data misfits onto the vertical coordinate. The other is a remote response generated by the propagation of barotropic Rossby waves away from the forcing area. The relative importance of these two responses on the dynamical balance in  $\mathbf{P}$  de-

pends on the latitude of the sample point  $(\mathbf{r}_m, t_m)$  and on the shape of the wind stress curl error covariance matrix.

This study does not resolve what proper functional form of the wind stress error covariance should be specified in a 4DVAR ocean data assimilation system. However, our results suggest an alternative approach in designing a wind stress error covariance. As discussed in appendix B, the wind stress error covariance functions can be constructed from the covariance functions of the wind stress curl and divergence. Although it is not clear how to design the wind stress curl and divergence error, the model state vector could be controlled more directly by choosing these errors as control parameters instead of the zonal and meridional wind stress errors. The

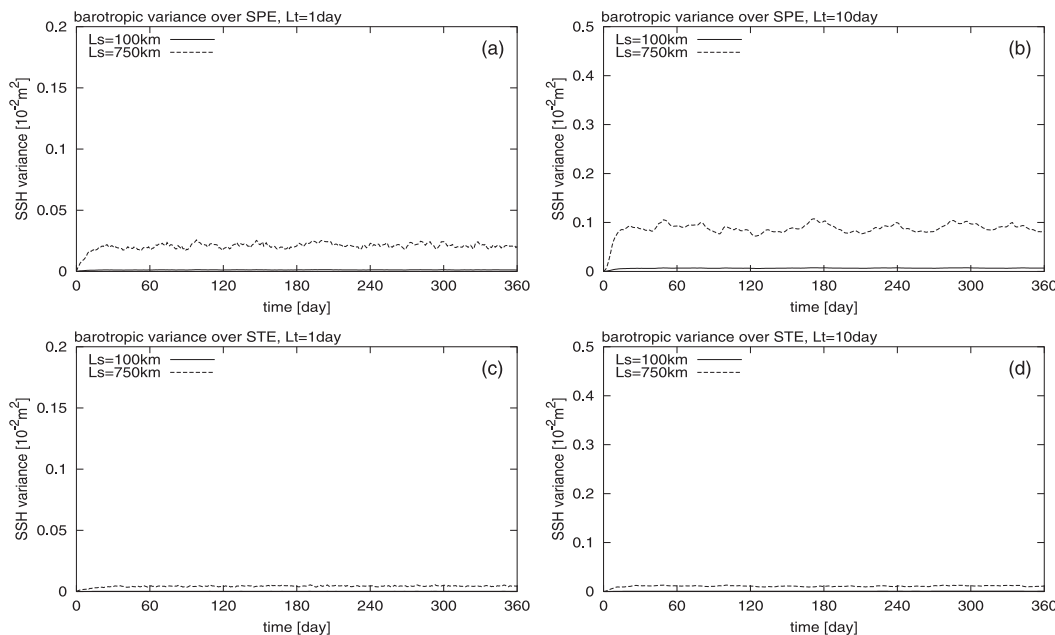


FIG. 9. As in Fig. 5, but computed for the barotropic model. Note that the amplitude of time series for  $L_S = 100$  km (continuous line) is too small to be clearly seen.

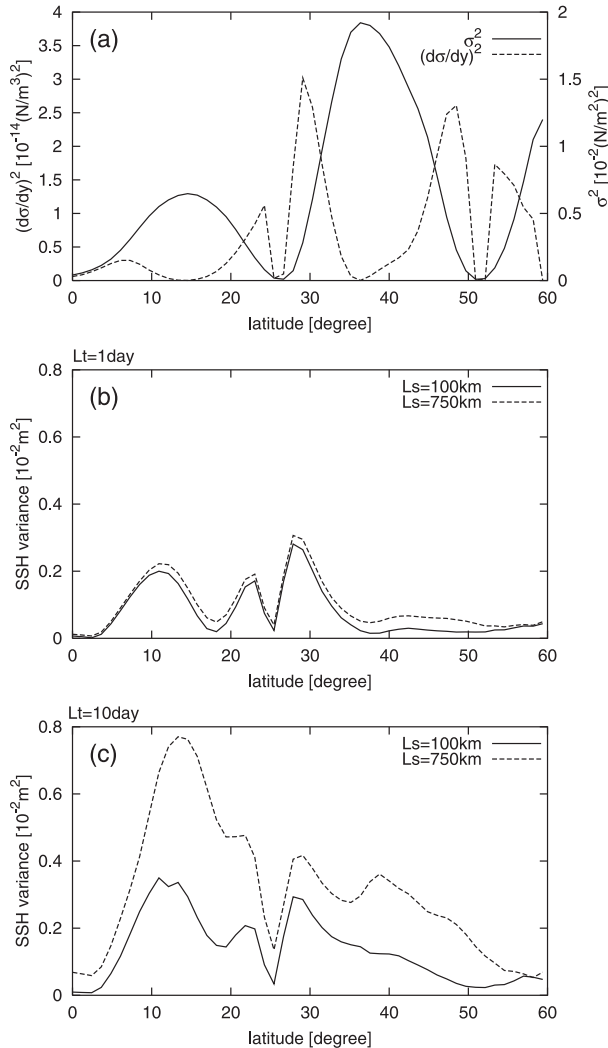


FIG. 10. (a) Meridional distribution of the variance of the wind stress error and the wind stress curl error in (41) and (45). The solid line is the variance of the zonal wind stress error  $\sigma_{\Delta\tau}^2$  and the dashed line is the variance of a meridional gradient of the zonal wind stress error  $(\partial\sigma_{\Delta\tau}/\partial y)^2$ . (b) Meridional distribution of zonally averaged SSH error variance at day 360 for  $L_T = 1$  day. (c) As in (b), but for  $L_T = 10$  days.

numerical implementation of such a scheme in a 4DVAR system using a generalized diffusion equation was proposed by Vossepoel et al. (2004; see appendix B).

It was also shown that for the wind stress perturbation over a 1-yr period, the statistics of the model state error do not reach a steady state, and this is because of the continuous growth of the baroclinic response. Considering the propagation speed of baroclinic Rossby waves, it is likely that these statistics will take another 10 yr to reach a steady state. Until that point, the dynamical balance in  $\mathbf{P}$  will change as the barotropic response converges to a steady state much earlier than the baro-

clinic response. For shorter assimilation windows of the order of 1 month, errors in the initial values are the major source of the model error  $\mathbf{u}$  that determines the dynamical balance in  $\mathbf{P}$  (e.g., Weaver et al. 2003). Our preliminary experiments, conducted with initial and wind stress errors, show that the SSH error variance is dominated by the initial error during the first 1 month period and the influence of the wind stress error takes over gradually thereafter. Since our results suggest that  $\mathbf{P}$  changes the dynamical balance depending on the length of the model perturbation period, further study would be required to define an optimal length of the assimilation window for each application.

*Acknowledgments.* We thank Andrew Bennett and Boon Chua for answering numerous questions on the use of their PEZ/IPEZ modeling system. The authors also thank two anonymous reviewers for their useful comments and suggestions. Financial support for this study was provided by both the Strategic Science Fund and the Centre for Ocean Model Development and Analysis (COMDA) from DFO and by the Canadian Foundation for Climate and Atmospheric Sciences (CFCAS) through the Global Ocean and Atmosphere Prediction and Predictability (GOAPP) Project.

## APPENDIX A

### Tangent Linear Equations in a Vector–Matrix Form

We assume that the tangent linear model derived from the nonlinear ocean circulation model in (5) consists of a set of prognostic equations as

$$\begin{cases} \mathbf{x}_0 = \mathbf{x}_0^b, \\ \mathbf{x}_1 = \mathbf{M}_{1,0}\mathbf{x}_0 + \tilde{\mathbf{f}}_1, \\ \vdots \\ \mathbf{x}_{N-1} = \mathbf{M}_{N-1,N-2}\mathbf{x}_{N-2} + \tilde{\mathbf{f}}_{N-1}, \end{cases} \quad (\text{A1})$$

where  $\mathbf{x}_n$  is the model state vector,  $\mathbf{x}_0^b$  is its initial value,  $\tilde{\mathbf{f}}_n$  is the extended forcing vector that includes the external forcing, boundary value and the pseudoforcing term arising from the linearization of a nonlinear dynamical operator. A vector with subscript  $n$  indicates that the vector is evaluated at time  $t_n$ . The matrix  $\mathbf{M}_{m,n}$  is called the transition matrix or the propagator between time  $t_m$  and  $t_n$ , which satisfies the following rule:

$$\mathbf{M}_{m,n} = \mathbf{M}_{m,m-1}\mathbf{M}_{m-1,m-2} \cdots \mathbf{M}_{n+1,n}, \quad \text{for } m - n \geq 1. \quad (\text{A2})$$

There are two approaches to summarize the tangent linear equations in (A1) in a single matrix equation. In

the first approach, we eliminate the term with model state vector  $\mathbf{x}_n$  from the right-hand side of (A1). Then we have a matrix equation

$$\mathbf{x} = \mathbf{M}\tilde{\mathbf{f}}, \tag{A3}$$

where

$$\mathbf{x} = \begin{bmatrix} \mathbf{x}_0 \\ \mathbf{x}_1 \\ \mathbf{x}_2 \\ \vdots \\ \mathbf{x}_{N-2} \\ \mathbf{x}_{N-1} \end{bmatrix}, \quad \mathbf{M} = \begin{bmatrix} \mathbf{I} & 0 & 0 & \cdots & 0 & 0 \\ \mathbf{M}_{1,0} & \mathbf{I} & 0 & \cdots & 0 & 0 \\ \mathbf{M}_{2,0} & \mathbf{M}_{2,1} & \mathbf{I} & \cdots & 0 & 0 \\ \vdots & \vdots & \vdots & \ddots & \vdots & \vdots \\ \mathbf{M}_{N-2,0} & \mathbf{M}_{N-2,1} & \mathbf{M}_{N-2,2} & \cdots & \mathbf{I} & 0 \\ \mathbf{M}_{N-1,0} & \mathbf{M}_{N-1,1} & \mathbf{M}_{N-1,2} & \cdots & \mathbf{M}_{N-1,N-2} & \mathbf{I} \end{bmatrix}, \quad \tilde{\mathbf{f}} = \begin{bmatrix} \mathbf{x}_0^b \\ \tilde{\mathbf{f}}_1 \\ \tilde{\mathbf{f}}_2 \\ \vdots \\ \tilde{\mathbf{f}}_{N-2} \\ \tilde{\mathbf{f}}_{N-1} \end{bmatrix}. \tag{A4}$$

In the second approach, we move the terms involving  $\mathbf{x}_n$  in (A1) from the right-hand side to the left-hand side of this equation. Then we obtain a matrix equation

$$\mathbf{G}\mathbf{x} = \tilde{\mathbf{f}}, \tag{A5}$$

where

$$\mathbf{G} = \begin{bmatrix} \mathbf{I} & 0 & 0 & \cdots & 0 & 0 \\ -\mathbf{M}_{1,0} & \mathbf{I} & 0 & \cdots & 0 & 0 \\ 0 & -\mathbf{M}_{2,1} & \mathbf{I} & \cdots & 0 & 0 \\ \vdots & \vdots & \vdots & \ddots & \vdots & \vdots \\ 0 & 0 & 0 & \cdots & \mathbf{I} & 0 \\ 0 & 0 & 0 & \cdots & -\mathbf{M}_{N-1,N-2} & \mathbf{I} \end{bmatrix}. \tag{A6}$$

Note that the matrices  $\mathbf{M}$  and  $\mathbf{G}$  are both lower triangular.

Since the two formulations, (A3) and (A5), are equivalent, the matrices  $\mathbf{M}$  and  $\mathbf{G}$  satisfy the following condition:

$$\mathbf{M}\mathbf{G} = \mathbf{G}\mathbf{M} = \mathbf{I}, \tag{A7}$$

that is,

$$\mathbf{M}^{-1} = \mathbf{G} \quad \text{and} \quad \mathbf{G}^{-1} = \mathbf{M}. \tag{A8}$$

The condition in (A7) can also be confirmed by direct multiplications between  $\mathbf{M}$  and  $\mathbf{G}$  as defined in (A4) and (A6). Note that the condition in (A7) is valid regardless of the formal invertibility of the transition matrix  $\mathbf{M}_{n,n-1}$ . From (A8) and (9), we obtain the identity equation

$$(\mathbf{M}\mathbf{Q}\mathbf{M}^T)^{-1} = \mathbf{G}^T\mathbf{Q}^{-1}\mathbf{G}, \tag{A9}$$

which is used to derive (10).

## APPENDIX B

### Error Covariance of a Wind Stress Field

From Eqs. (24) and (25), the auto- and cross-covariance functions of the wind stress curl error and the wind stress divergence error can be expressed in terms of the auto- and cross-covariance functions of the wind stress error as

$$\begin{aligned} Q_{\Delta s \Delta s}(\mathbf{r}_1; \mathbf{r}_2) &= \frac{\partial^2 Q_{\Delta \tau}^{yy}(\mathbf{r}_1; \mathbf{r}_2)}{\partial x_1 \partial x_2} - \frac{\partial^2 Q_{\Delta \tau}^{yx}(\mathbf{r}_1; \mathbf{r}_2)}{\partial x_1 \partial y_2} - \frac{\partial^2 Q_{\Delta \tau}^{xy}(\mathbf{r}_1; \mathbf{r}_2)}{\partial y_1 \partial x_2} + \frac{\partial^2 Q_{\Delta \tau}^{xx}(\mathbf{r}_1; \mathbf{r}_2)}{\partial y_1 \partial y_2}, \\ Q_{\Delta \mu \Delta \mu}(\mathbf{r}_1; \mathbf{r}_2) &= \frac{\partial^2 Q_{\Delta \tau}^{xx}(\mathbf{r}_1; \mathbf{r}_2)}{\partial x_1 \partial x_2} + \frac{\partial^2 Q_{\Delta \tau}^{xy}(\mathbf{r}_1; \mathbf{r}_2)}{\partial x_1 \partial y_2} + \frac{\partial^2 Q_{\Delta \tau}^{yx}(\mathbf{r}_1; \mathbf{r}_2)}{\partial y_1 \partial x_2} + \frac{\partial^2 Q_{\Delta \tau}^{yy}(\mathbf{r}_1; \mathbf{r}_2)}{\partial y_1 \partial y_2}, \\ Q_{\Delta s \Delta \mu}(\mathbf{r}_1; \mathbf{r}_2) &= \frac{\partial^2 Q_{\Delta \tau}^{yx}(\mathbf{r}_1; \mathbf{r}_2)}{\partial x_1 \partial x_2} + \frac{\partial^2 Q_{\Delta \tau}^{yy}(\mathbf{r}_1; \mathbf{r}_2)}{\partial x_1 \partial y_2} - \frac{\partial^2 Q_{\Delta \tau}^{xx}(\mathbf{r}_1; \mathbf{r}_2)}{\partial y_1 \partial x_2} - \frac{\partial^2 Q_{\Delta \tau}^{xy}(\mathbf{r}_1; \mathbf{r}_2)}{\partial y_1 \partial y_2}, \quad \text{and} \\ Q_{\Delta \mu \Delta s}(\mathbf{r}_1; \mathbf{r}_2) &= \frac{\partial^2 Q_{\Delta \tau}^{xy}(\mathbf{r}_1; \mathbf{r}_2)}{\partial x_1 \partial x_2} - \frac{\partial^2 Q_{\Delta \tau}^{xx}(\mathbf{r}_1; \mathbf{r}_2)}{\partial x_1 \partial y_2} + \frac{\partial^2 Q_{\Delta \tau}^{yy}(\mathbf{r}_1; \mathbf{r}_2)}{\partial y_1 \partial x_2} - \frac{\partial^2 Q_{\Delta \tau}^{yx}(\mathbf{r}_1; \mathbf{r}_2)}{\partial y_1 \partial y_2}. \end{aligned} \tag{B1}$$

These equations correspond to the functional relation in (26).

We now closely follow the discussion about the wind error covariance in Daley (1991). For simplicity, we assume that the stochastic processes only depend on the two-dimensional spatial coordinates for the sea surface. The wind stress error field can be related to the scalar variables using the Helmholtz's theorem as

$$\Delta\tau_x = -\frac{\partial\psi}{\partial y} + \frac{\partial\chi}{\partial x} \quad \text{and} \quad \Delta\tau_y = \frac{\partial\psi}{\partial x} + \frac{\partial\chi}{\partial y}, \quad (\text{B2})$$

where  $\psi$  is the scalar potential that controls the rotational component (curl) in the wind stress error and  $\chi$  is the vector potential that controls its irrotational component (divergence). Wind stress curl error  $\Delta\varsigma$  and wind stress divergence error  $\Delta\mu$  can be recovered from  $\psi$  and  $\chi$  as

$$\Delta\varsigma = \nabla^2\psi \quad \text{and} \quad \Delta\mu = \nabla^2\chi, \quad (\text{B3})$$

where  $\nabla^2 \equiv \partial^2/\partial x^2 + \partial^2/\partial y^2$ . From (B2), the components of the covariance functions of the wind stress error can be written in terms of covariance functions of the two scalar variables  $\psi$  and  $\chi$  as

$$\begin{aligned} Q_{\Delta\tau}^{xx}(\mathbf{r}_1; \mathbf{r}_2) &= \frac{\partial^2 Q_{\psi\psi}(\mathbf{r}_1; \mathbf{r}_2)}{\partial y_1 \partial y_2} + \frac{\partial^2 Q_{\chi\chi}(\mathbf{r}_1; \mathbf{r}_2)}{\partial x_1 \partial x_2} - \frac{\partial^2 Q_{\psi\chi}(\mathbf{r}_1; \mathbf{r}_2)}{\partial y_1 \partial x_2} - \frac{\partial^2 Q_{\chi\psi}(\mathbf{r}_1; \mathbf{r}_2)}{\partial x_1 \partial y_2}, \\ Q_{\Delta\tau}^{yy}(\mathbf{r}_1; \mathbf{r}_2) &= \frac{\partial^2 Q_{\psi\psi}(\mathbf{r}_1; \mathbf{r}_2)}{\partial x_1 \partial x_2} + \frac{\partial^2 Q_{\chi\chi}(\mathbf{r}_1; \mathbf{r}_2)}{\partial y_1 \partial y_2} + \frac{\partial^2 Q_{\psi\chi}(\mathbf{r}_1; \mathbf{r}_2)}{\partial x_1 \partial y_2} + \frac{\partial^2 Q_{\chi\psi}(\mathbf{r}_1; \mathbf{r}_2)}{\partial y_1 \partial x_2}, \\ Q_{\Delta\tau}^{xy}(\mathbf{r}_1; \mathbf{r}_2) &= -\frac{\partial^2 Q_{\psi\psi}(\mathbf{r}_1; \mathbf{r}_2)}{\partial y_1 \partial x_2} + \frac{\partial^2 Q_{\chi\chi}(\mathbf{r}_1; \mathbf{r}_2)}{\partial x_1 \partial y_2} - \frac{\partial^2 Q_{\psi\chi}(\mathbf{r}_1; \mathbf{r}_2)}{\partial y_1 \partial y_2} + \frac{\partial^2 Q_{\chi\psi}(\mathbf{r}_1; \mathbf{r}_2)}{\partial x_1 \partial x_2}, \quad \text{and} \\ Q_{\Delta\tau}^{yx}(\mathbf{r}_1; \mathbf{r}_2) &= -\frac{\partial^2 Q_{\psi\psi}(\mathbf{r}_1; \mathbf{r}_2)}{\partial x_1 \partial y_2} + \frac{\partial^2 Q_{\chi\chi}(\mathbf{r}_1; \mathbf{r}_2)}{\partial y_1 \partial x_2} + \frac{\partial^2 Q_{\psi\chi}(\mathbf{r}_1; \mathbf{r}_2)}{\partial x_1 \partial x_2} - \frac{\partial^2 Q_{\chi\psi}(\mathbf{r}_1; \mathbf{r}_2)}{\partial y_1 \partial y_2}. \end{aligned} \quad (\text{B4})$$

From (B3), the covariance functions of  $\psi$  and  $\chi$  are

$$\begin{aligned} Q_{\psi\psi}(\mathbf{r}_1; \mathbf{r}_2) &= \nabla_1^{-2} \nabla_2^{-2} Q_{\Delta\varsigma\Delta\varsigma}(\mathbf{r}_1; \mathbf{r}_2), \\ Q_{\chi\chi}(\mathbf{r}_1; \mathbf{r}_2) &= \nabla_1^{-2} \nabla_2^{-2} Q_{\Delta\mu\Delta\mu}(\mathbf{r}_1; \mathbf{r}_2), \\ Q_{\psi\chi}(\mathbf{r}_1; \mathbf{r}_2) &= \nabla_1^{-2} \nabla_2^{-2} Q_{\Delta\varsigma\Delta\mu}(\mathbf{r}_1; \mathbf{r}_2), \quad \text{and} \\ Q_{\chi\psi}(\mathbf{r}_1; \mathbf{r}_2) &= \nabla_1^{-2} \nabla_2^{-2} Q_{\Delta\mu\Delta\varsigma}(\mathbf{r}_1; \mathbf{r}_2). \end{aligned} \quad (\text{B5})$$

Equations (B4) and (B5) establish the functional relationship in (27).

When we assume that  $Q_{\psi\chi} = Q_{\chi\psi} = 0$ , (B4) indicates that we can parameterize the wind stress error covariance functions only by the two covariance functions,

$Q_{\psi\psi}$  and  $Q_{\chi\chi}$ . Convolution between the wind stress error covariance and adjoint variables on the right-hand side of (16) can be written in the continuous form as

$$\begin{aligned} &\iint \mathbf{Q}_{\Delta\tau}(\mathbf{r}_1; \mathbf{r}_2) \boldsymbol{\lambda}(\mathbf{r}_2) \, d\mathbf{r}_2 \\ &= \iint \begin{bmatrix} Q_{\Delta\tau}^{xx}(\mathbf{r}_1; \mathbf{r}_2) & Q_{\Delta\tau}^{xy}(\mathbf{r}_1; \mathbf{r}_2) \\ Q_{\Delta\tau}^{yx}(\mathbf{r}_1; \mathbf{r}_2) & Q_{\Delta\tau}^{yy}(\mathbf{r}_1; \mathbf{r}_2) \end{bmatrix} \begin{bmatrix} \lambda_x \\ \lambda_y \end{bmatrix} \, d\mathbf{r}_2, \end{aligned} \quad (\text{B6})$$

where  $\lambda_{x(y)}$  is the adjoint variable. For simplicity, we omit the time coordinate. With the assumptions that  $Q_{\psi\chi} = Q_{\chi\psi} = 0$  in (B4), the convolution in (B6) can be expressed in the relatively simple formulation

$$\iint \mathbf{Q}_{\Delta\tau}(\mathbf{r}_1; \mathbf{r}_2) \boldsymbol{\lambda}(\mathbf{r}_2) \, d\mathbf{r}_2 = \begin{bmatrix} -\frac{\partial}{\partial y_1} & \frac{\partial}{\partial x_1} \\ \frac{\partial}{\partial x_1} & \frac{\partial}{\partial y_1} \end{bmatrix} \begin{bmatrix} \iint Q_{\psi\psi}(\mathbf{r}_1; \mathbf{r}_2) \lambda_\psi(\mathbf{r}_2) \, d\mathbf{r}_2 \\ \iint Q_{\chi\chi}(\mathbf{r}_1; \mathbf{r}_2) \lambda_\chi(\mathbf{r}_2) \, d\mathbf{r}_2 \end{bmatrix}, \quad (\text{B7})$$

where

$$\lambda_\psi = -\frac{\partial\lambda_y}{\partial x} + \frac{\partial\lambda_x}{\partial y}, \quad \lambda_\chi = -\frac{\partial\lambda_x}{\partial x} - \frac{\partial\lambda_y}{\partial y}, \quad (\text{B8})$$

and we have assumed that  $Q_{\psi\psi(\chi\chi)} \rightarrow 0$  as  $|\mathbf{r}_1 - \mathbf{r}_2| \rightarrow \infty$ . Since the two convolutions on the right-hand side of

(B7) are univariate operations, they can be easily implemented in the 4DVAR system when the covariances  $Q_{\psi\psi}$  and  $Q_{\chi\chi}$  are modeled by the generalized diffusion equation (Weaver and Courtier 2001). A similar scheme was implemented by Vossepoel et al. (2004) in their 4DVAR system to adjust a wind stress error in their equatorial Pacific Ocean circulation model.

## REFERENCES

- Bennett, A. F., 1992: *Inverse Methods in Physical Oceanography*. Cambridge University Press, 347 pp.
- , 2002: *Inverse Modeling of the Ocean and Atmosphere*. Cambridge University Press, 234 pp.
- , and M. A. Thorburn, 1992: The generalized inverse of a nonlinear quasi-geostrophic ocean circulation model. *J. Phys. Oceanogr.*, **22**, 213–231.
- Chua, B. S., and A. F. Bennett, 2001: An inverse ocean modeling system. *Ocean Modell.*, **3**, 137–165.
- Conkright, M. E., R. A. Locarnini, H. E. Garcia, T. D. O'Brien, T. P. Boyer, C. Stephens, and J. I. Antonov, 2002: World Ocean Atlas 2001: Objective analyses, data statistics, and figures. CD-ROM documentation, National Oceanographic Data Center, Silver Spring, MD, 17 pp.
- Courtier, P., 1997: Dual formulation of four-dimensional variational assimilation. *Quart. J. Roy. Meteor. Soc.*, **123**, 2449–2461.
- Cox, M. D., 1984: A primitive equation, 3-dimensional model of the ocean. GFDL Ocean Group Tech. Rep. 1, 250 pp.
- , and K. Bryan, 1984: A numerical model of the ventilated thermocline. *J. Phys. Oceanogr.*, **14**, 674–687.
- Daley, R., 1991: *Atmospheric Data Analysis*. Cambridge University Press, 457 pp.
- Fukumori, I., R. Raghunath, L.-L. Fu, and Y. Chao, 1999: Assimilation of TOPEX/POSEIDON altimeter data into a global ocean circulation model: How good are the results? *J. Geophys. Res.*, **104**, 25 647–25 665.
- Frankignoul, C., P. Müller, and E. Zorita, 1997: A simple model of the decadal response of the ocean to stochastic wind forcing. *J. Phys. Oceanogr.*, **27**, 1533–1546.
- Gille, S. T., 2005: Statistical characterization of zonal and meridional ocean wind stress. *J. Atmos. Oceanic Technol.*, **22**, 1353–1372.
- Köhl, A., D. Stammer, and B. Cornuelle, 2007: Interannual to decadal changes in the ECCO global synthesis. *J. Phys. Oceanogr.*, **37**, 313–337.
- Lorenc, A. C., 2003: Modelling of error covariances by 4D-Var data assimilation. *Quart. J. Roy. Meteor. Soc.*, **129**, 3167–3182.
- Masuda, S., T. Awaji, N. Sugiura, Y. Ishikawa, K. Baba, K. Horiuchi, and N. Komori, 2003: Improved estimates of the dynamical state of the North Pacific Ocean from a 4 dimensional variational data assimilation. *Geophys. Res. Lett.*, **30**, 1868, doi:10.1029/2003GL017604.
- Miller, R. N., and M. A. Cane, 1989: A Kalman filter analysis of sea level height in the tropical Pacific. *J. Phys. Oceanogr.*, **19**, 773–790.
- Milliff, R. F., J. Morzel, D. B. Chelton, and M. H. Freilich, 2004: Wind stress curl and wind stress divergence biases from rain effects on QSCAT surface wind retrievals. *J. Atmos. Oceanic Technol.*, **21**, 1216–1231.
- Muccino, J. C., and Coauthors, 2008: The Inverse Ocean Modeling System. Part II: Applications. *J. Atmos. Oceanic Technol.*, **25**, 1623–1637.
- Müller, P., and C. Frankignoul, 1981: Direct atmospheric forcing of geostrophic eddies. *J. Phys. Oceanogr.*, **11**, 287–308.
- Ngodock, H. E., B. S. Chua, and A. F. Bennett, 2000: Generalized inverse of a reduced gravity primitive equation ocean model and tropical atmosphere–ocean data. *Mon. Wea. Rev.*, **128**, 1757–1777.
- Pacanowski, R. C., and S. M. Griffies, 1999: The MOM3 manual. GFDL Ocean Group Tech. Rep. 4, NOAA/Geophysical Fluid Dynamics Laboratory, Princeton, NJ, 680 pp.
- Priestley, M. B., 1981: *Spectral Analysis and Time Series*. Vol. 1, Academic Press, 702 pp.
- Stammer, D., and Coauthors, 2002: The global ocean circulation during 1992–1997, estimated from ocean observations and a general circulation model. *J. Geophys. Res.*, **107**, 3118, doi:10.1029/2001JC000888.
- , and Coauthors, 2003: Volume, heat, and freshwater transports of the global ocean circulation 1993–2000, estimated from a general circulation model constrained by World Ocean Circulation Experiment (WOCE) data. *J. Geophys. Res.*, **108**, 3007, doi:10.1029/2001JC001115.
- Todling, R., 2000: Estimation theory and atmospheric data assimilation. *Inverse Methods in Global Biogeochemical Cycles*, *Geophys. Monogr.*, Vol. 114, Amer. Geophys. Union, 49–65.
- Trenberth, K. E., J. G. Olson, and W. G. Large, 1989: A global ocean wind stress climatology based on ECMWF analyses. NCAR Tech. Note NCAR/TN-338+STR, 93 pp.
- Veronis, G., 1970: Effect of fluctuating wind on ocean circulation. *Deep-Sea Res.*, **17**, 421–434.
- , and H. Stommel, 1956: The action of variable wind stresses on a stratified ocean. *J. Mar. Res.*, **15**, 43–75.
- Vialard, J., F. Vitart, M. Balmaseda, T. Stockdale, and D. Anderson, 2005: An ensemble generation method for seasonal forecasting with an ocean–atmosphere coupled model. *Mon. Wea. Rev.*, **133**, 441–453.
- Vossepoel, F. C., A. T. Weaver, J. Vialard, and P. Delecluse, 2004: Adjustment of near-equatorial wind stress with four-dimensional variational data assimilation in a model of the Pacific Ocean. *Mon. Wea. Rev.*, **132**, 2070–2083.
- Weaver, A. T., and P. Courtier, 2001: Correlation modelling on the sphere using a generalized diffusion equation. *Quart. J. Roy. Meteor. Soc.*, **127**, 1815–1846.
- , J. Vialard, and D. L. T. Anderson, 2003: Three- and four-dimensional variational assimilation in a general circulation model of the tropical Pacific Ocean. Part I: Formulation, internal diagnostics, and consistency checks. *Mon. Wea. Rev.*, **131**, 1360–1378.
- Willebrand, J., S. G. H. Philander, and R. C. Pacanowski, 1980: The oceanic response to large-scale atmospheric disturbances. *J. Phys. Oceanogr.*, **10**, 411–429.